CrossMark

ORIGINAL PAPER

A. S. Pavan Kumar · Satyajit Panda · N. H. Reddy

Smart damping of vibration of annular plates by the design of a cylindrically orthotropic piezoelectric fiber-reinforced composite actuator

Abstract In the present work, the active control of vibration of annular plates is presented by the design of a cylindrically orthotropic short/continuous piezoelectric fiber-reinforced composite (SPFRC/CPFRC) actuator. The unidirectional piezoelectric fibers of the smart composite are oriented along the radial direction within a reference cylindrical coordinate frame and poled in the same direction. First, a finite element analysis of the effective electro-elastic properties of the smart composite is presented, and the optimal geometry of its unit cell is determined with an objective of improved magnitude of an effective piezoelectric coefficient (e_{11}, 1 for radial direction) for both short (SPFRC) and continuous (CPFRC) forms of piezoelectric fibers. Next, an arrangement of surface electrodes is presented for its effectual utilization as an actuator based on the coefficient e_{11}. Subsequently, the smart actuator is attached to the surface of a host annular plate in the form of actuator patches for substantiating its control performance by the numerical evaluation of controlled frequency responses of the overall smart annular plate. The actuator patches act as smart dampers by means of supplying voltage according to the velocity feedback control strategy. The numerical results reveal more control power of the SPFRC actuator than that of a CPFRC actuator even though the magnitude of the major effective coefficient (e_{11}) for SPFRC is lesser than that for CPFRC. The overall analysis shows a meaningful control power of present cylindrically orthotropic SPFRC/CPFRC actuators in control of vibration of annular plates and suggests short piezoelectric fibers instead of continuous fibers within it (smart actuator) for achieving its larger control power, flexibility and conformability.

1 Introduction

The property of piezoelectric ceramics to produce an electric field by exerting mechanical stress/strain and vice versa is known as piezoelectricity. These direct and converse piezoelectric effects of piezoelectric ceramics are exploited in the development of distributed piezoelectric sensors and actuators for structural applications [1,2]. The piezoelectric sensors and actuators are normally attached to or embedded in the host structure [3] in order to accomplish self-sensing and self-controlling capabilities of the entire structure. Such structures are known as 'smart structures.' Over the past two decades, the concept of a smart structure has been frequently utilized for active control of vibration of various flexible structural elements like beams, plates, shells, circular/annular plates, etc. [3–13]. In this development of a smart structure, monolithic piezoelectric materials are extensively employed as materials for distributed sensors and actuators. However, the control power of monolithic piezoelectric ceramics is very low due to small magnitudes of piezoelectric stress/strain coefficients. The monolithic piezoelectric ceramics also suffer from various demerits such as low flexibility, high stiffness, low strain and

A. S. Pavan Kumar · S. Panda (✉) · N. H. Reddy
Department of Mechanical Engineering, Indian Institute of Technology Guwahati, North Guwahati,
Guwahati 781039, Assam, India
E-mail: spanda@iitg.ernet.in
Tel.: 91-361-2582664

energy density [14–16]. These disadvantages in the utilization of monolithic piezoelectric actuators are cared by many researchers resulting in various piezoelectric fiber-reinforced composites (PFRCs) [17–26]. Among the different piezoelectric composites, the microfiber composite (MFC) and the active-fiber composite (AFC) [19,20] are popular smart composite materials for distributed actuators in control of structural vibration. The AFC/MFC actuator consists of unidirectional continuous monolithic piezoelectric fibers (longitudinally poled) embedded within the polymer matrix. The special arrangement of inter-digitized electrodes (IDE) on the top and bottom surfaces of AFC/MFC results in an electrically induced actuation force along the longitudinal direction of the fibers. Because of the uses of a polymer matrix and thin piezoelectric fibers, an AFC/MFC actuator is a more flexible and conformable actuator than a monolithic piezoelectric actuator [27]. As a consequence, the use of continuous piezoelectric fibers in smart composite actuators may cause difficulties in their practical structural applications, especially when the overall smart structure undergoes large/nonlinear deformation or when the actuator is to be integrated over the curved surface of the host structure. The thin, brittle and long piezoelectric fibers within the actuator may break in these cases and this may eventually hamper its control performance. For avoiding these practical difficulties, the smart actuator may be used in the form of a patch. But the aforesaid shortcomings persist depending on the size of the actuator patch and also on the location of the same over the curved surface of the host structure. Another possible option is to use short piezoelectric fibers instead of continuous fibers. By the use of short fibers, all the aforesaid shortcomings can be eliminated along with the advantages of enhanced flexibility and conformability of a smart composite actuator. Although these advantages can be achieved by the use of short piezoelectric fibers instead of continuous fibers, the corresponding change in the magnitudes of the effective piezoelectric coefficients is a major concern for its (smart composite) use as an actuator in structural applications. So, the use of short piezoelectric fibers in the design of a smart composite actuator not only provides the aforesaid advantages but also imposes a critical aspect of the magnitudes of effective piezoelectric coefficients.

The different piezoelectric composite actuators including MFC/AFC actuators are substantially employed in control of vibration of various host structures such as beams, plates, shells and airfoils [28–36]. Similar to these structural elements, the plane structures of revolution like circular and annular plates are also equally important structural elements for their wide applications in different engineering fields. For controlling flexural modes of vibration of such plane structures of revolution, any of the existing piezoelectric composite actuators may be utilized. It may not be an effective use of existing smart composite actuators. Because, the microstructure of any of the existing piezoelectric composite actuators is designed based on a specific coordinate frame and also it is for controlling a specific mode of deformation of the host structure. Since none of the available piezoelectric composite actuators is specially designed for controlling the flexural vibration of plane structures of revolution, presently a cylindrically orthotropic piezoelectric fiber-reinforced composite (PFRC) actuator is designed and analyzed for its control performance.

In the present work, a cylindrically orthotropic PFRC actuator is designed for its utilization in control of the vibration of annular plates. The smart composite is comprised of unidirectional piezoelectric fibers embedded within the epoxy matrix. The fibers are oriented along the radial direction within the reference cylindrical coordinate frame and also poled in the same direction so as to achieve an improved magnitude of an effective piezoelectric coefficient (e_{11}, 1 for the radial direction). The piezoelectric fibers are first considered in continuous form (CPFRC). Next, the same fibers are considered in a discontinuous form (SPFRC) to constitute unidirectional short piezoelectric fibers along the radial direction. For both the forms of piezoelectric fibers, the effective electro-elastic properties of the cylindrically orthotropic PFRC are evaluated using a finite element (FE) procedure. A numerical analysis of effective properties is performed in order to determine the geometrical dimensions of the corresponding representative volume element (RVE) with an objective of improved magnitude of the major effective piezoelectric coefficient (e_{11}). For effective utilization of the major piezoelectric coefficient (e_{11}) of the SPFRC/CPFRC, the arrangement of surface electrodes over the top and bottom surfaces of the composite layer is presented. Subsequently, its (SPFRC/CPFRC actuator) control performance is substantiated by the vibration analysis of an annular plate integrated with the patches of the same (SPFRC/CPFRC) actuator. Specifically, the change in the control performance of the present cylindrically orthotropic PFRC actuator due to the use of short piezoelectric fibers (SPFRC) instead of continuous fibers (CPFRC) is investigated considering the same arrangement of surface electrodes. To the best knowledge of the authors, similar design and analysis of cylindrically orthotropic SPFRC actuators for controlling the vibration of plane structures of revolution are not yet available in the literature.

2 Present cylindrically orthotropic SPFRC

Figure 1a shows a schematic diagram of a present cylindrically orthotropic unidirectional short piezoelectric fiber-reinforced composite (SPFRC). The short piezoelectric fibers have identical dimension along every axial direction (r, θ, z) in the reference polar coordinate frame. Also, the fibers are equally spaced along all axial (r, θ, z) directions. The fiber and matrix phases are made of monolithic piezoelectric and elastic epoxy materials, respectively. All short piezoelectric fibers are poled along the radial direction and assumed to be perfectly bonded to the matrix phase. Since the analysis of a composite material for the determination of its effective material constants is generally confined to a unit cell or representative volume element (RVE), a similar element for the present smart composite is considered as illustrated in Fig. 1b. The short piezoelectric fiber is centrally located within the volume of the RVE. The inner/outer radius of the RVE and the corresponding short fiber are denoted by r_i^c/r_o^c and r_i^f/r_o^f, respectively. So, the symbols l_c and l_f in Fig. 1b stand for the radial lengths of RVE and corresponding fiber, respectively. The circumferential span of RVE/fiber is designated by θ_c/θ_f, while the thickness of the same is symbolized by h_c/h_f. The volume fractions of fiber and matrix phases within the volume of the RVE are represented by the symbols v_f and v_m, respectively. Because of the short fiber, the fiber volume fraction can be expressed as $v_f = (A_r \times L_r)(L_r = l_f/l_c, \ A_r = \langle\theta_f h_f\rangle/\langle\theta_c h_c\rangle)$. The parameter (A_r) is basically the cross-sectional area ratio (A_f/A_c) between the fiber and the RVE at any radius (r), while the parameter (L_r) signifies the ratio of their radial lengths. The dimensions of RVE and corresponding fiber in the θz-plane at any radius are considered to be related to $(h_f/h_c) = (\theta_f/\theta_c)$ so that the area ratio (A_r) may be expressed either by $(\theta_f/\theta_c)^2$ or by $(h_f/h_c)^2$. Alternatively, the dimensions (h_f, θ_f) of the fiber may be expressed in terms of the similar dimensions (h_c, θ_c) of RVE as $h_f = h_c\sqrt{A_r}$ and $\theta_f = \theta_c\sqrt{A_r}$. However, according to the aforesaid geometrical relations, all dimensions of the RVE can be specified by L_r, A_r, h_c, θ_c and l_c. A boundary surface of RVE is denoted by its normal direction. So, the six boundary surfaces of the RVE are denoted by $-r$, $+r$, $-\theta$, $+\theta$, $-z$ and $+z$ surfaces.
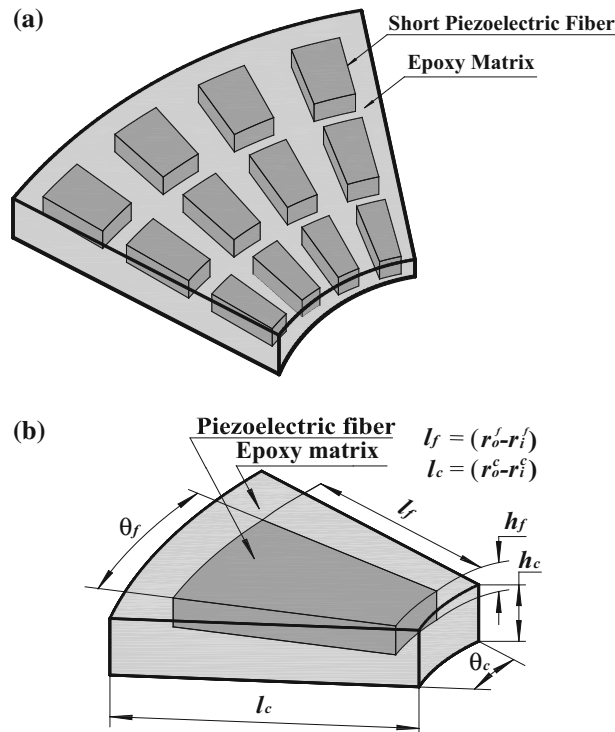

Fig. 1 a Schematic diagram of the present cylindrically orthotropic radially poled short piezoelectric fiber reinforced composite, **b** the corresponding representative volume element (RVE)

3 Effective electro-elastic constants of the piezoelectric composite

In the theory of linear piezoelectricity without thermal effect, the coupled interaction between the electric and elastic fields is described by four different piezoelectric constitutive formulations [37,38]. Among these four different constitutive formulations, the piezoelectric stress formulation is commonly employed when the strain and electric fields are considered as natural variables. According to this constitutive formulation, the natural variables (strain and electric fields) are related to the stress and electric displacement fields by

$$\sigma_{ij} = C_{ijkl}\varepsilon_{kl} - e_{sij}E_s, \, D_i = e_{ikl}\varepsilon_{kl} + \in_{is} E_s \tag{1}$$

where $i, j, k, l, s = 1, 2, 3$; C_{ijkl}, e_{sij} and $\in_{is}$ denote the elements of stiffness, piezoelectric and permittivity tensors, respectively; σ_{ij}, ε_{kl}, D_i and E_s are the elements of stress, strain, electric displacement and electric field tensors, respectively. In Eq. (1), the mathematical objects are symmetric in i and j, and also in k and l. So, using Voigt notation, ij/kl for $i, j, k, l = 1, 2, 3$ could be represented as $11 \rightarrow 1$, $22 \rightarrow 2$, $33 \rightarrow 3$, $23/32 \rightarrow 4$, $13/31 \rightarrow 5$ and $12/21 \rightarrow 6$. Using this notation, Eq. (1) can be rewritten as

$$\sigma_\xi = C_{\xi\eta}\varepsilon_\eta - e_{\ell\xi}E_\ell, \, D_\ell = e_{\ell\eta}\varepsilon_\eta + \in_{\ell\zeta} E_\zeta \tag{2}$$

where $\xi, \eta = 1, 2, 3, 4, 5, 6$ and $\ell, \zeta = 1, 2, 3$. In Eq. (2), the elements of stiffness, piezoelectric and permittivity matrices are defined by [39,40]

$$C_{\xi\eta} = \left(\frac{\partial\sigma_\xi}{\partial\varepsilon_\eta}\right)^E, e_{\ell\xi} = -\left(\frac{\partial\sigma_\xi}{\partial E_\ell}\right)^\varepsilon \text{ or } e_{\ell\eta} = \left(\frac{\partial D_\ell}{\partial\varepsilon_\eta}\right)^E, \in_{\ell\zeta} = \left(\frac{\partial D_\ell}{\partial E_\zeta}\right)^\varepsilon. \tag{3}$$

The superscript E [Eq. (3)] indicates a zero or constant electric field, and the superscript ε [Eq. (3)] indicates zero or constant strain field. The constitutive relations and material constants in Eqs. (2) and (3), respectively, are given for a perfect homogeneous piezoelectric solid. Analogous to this homogeneous piezoelectric solid, the present piezoelectric composite is considered to be a macroscopically homogeneous piezoelectric solid, and its macroscopic behavior can be defined by effective constitutive relations according to standard micromechanical theories for composites. These effective constitutive relations are valid only for specially statistically homogeneous fields within the composite, which (fields) can be produced within a heterogeneous body by the imposition of homogeneous boundary conditions over the boundary surfaces of the body [41,42]. Making use of this analogy, the effective material properties of asymptotically homogeneous composites could be estimated by the application of volume-average strain field and/or electric field by means of homogeneous kinematic boundary conditions (displacement and/or electric potential) [43]. Following that at present, the effective material constants of the piezoelectric composite are estimated by applying RVE volume-average strain field and/or electric field. The volume-average field quantities over a volume (V_d) are defined by

$$\overline{\sigma}_\xi = \frac{1}{V_d}\int_{V_d}\sigma_\xi dV_d, \overline{\varepsilon}_\eta = \frac{1}{V_d}\int_{V_d}\varepsilon_\eta dV_d, \overline{E}_\ell = \frac{1}{V_d}\int_{V_d}E_\ell dV_d, \overline{D}_\zeta = \frac{1}{V}\int_V D_\zeta dV \tag{4}$$

where the over-bar signifies a volume-average quantity. Equation (4) indicates general expressions for the volume averages of field quantities. These expressions could be utilized for any volume among the volumes of the RVE, fiber phase and matrix phase by specifying the corresponding fields (σ_ξ, ε_η, E_ℓ, D_ζ) and volume (V_d). The constitutive relations for fiber (f) and matrix (m) phase materials within the RVE can be written in terms of the volume-average field quantities as follows:

$$\overline{\sigma}_\xi^f = C_{\xi\eta}^f\overline{\varepsilon}_\eta^f - e_{\ell\xi}^f\overline{E}_\ell^f, \tag{5}$$

$$\overline{\sigma}_\xi^m = C_{\xi\eta}^m\overline{\varepsilon}_\eta^m, \tag{6}$$

$$\overline{D}_\ell^f = e_{\ell\eta}^f\overline{\varepsilon}_\eta^f + \in_{\ell\zeta}^f \overline{E}_\zeta^f, \tag{7}$$

$$\overline{D}_\ell^m = \in_{\ell\zeta}^m \overline{E}_\zeta^m. \tag{8}$$

The volume-average field quantities of the RVE could be expressed in terms of the similar quantities of constituent phases as follows:

$$\overline{\sigma}_\xi = \left(v_f\overline{\sigma}_\xi^f + v_m\overline{\sigma}_\xi^m\right), \tag{9}$$

$$\overline{D}_\ell = \left(v_f\overline{D}_\ell^f + v_m\overline{D}_\ell^m\right), \tag{10}$$

$$\overline{\varepsilon}_\eta = \left(v_f\overline{\varepsilon}_\eta^f + v_m\overline{\varepsilon}_\eta^m\right), \tag{11}$$

$$\overline{E}_\zeta = \left(v_f\overline{E}_\zeta^f + v_m\overline{E}_\zeta^m\right). \tag{12}$$

Substituting Eqs. (5)–(6) in Eq. (9) and then using Eq. (11), the following expression can be obtained:

$$\overline{\sigma}_\xi = C_{\xi\alpha}^m\overline{\varepsilon}_\alpha + v_f\left(C_{\xi\alpha}^f - C_{\xi\alpha}^m\right)\overline{\varepsilon}_\alpha^f - v_f e_{\ell\xi}^f\overline{E}_\ell^f \tag{13}$$

where $\alpha = 1, 2, 3, 4, 5, 6$. Similarly, substituting Eqs. (7)–(8) into Eq. (10) and then using Eq. (12), the following expression can be obtained:

$$\overline{D}_\ell = \in_{\ell\beta}^m \overline{E}_\beta + v_f\left(\in_{\ell\beta}^f - \in_{\ell\beta}^m\right)\overline{E}_\beta^f + v_f e_{\ell\eta}^f\overline{\varepsilon}_\eta^f \tag{14}$$

where $\beta = 1, 2, 3$. According to the definitions of piezoelectric constants [Eq. (3)], the following expressions for the effective electro-elastic constants of the piezoelectric composite can be obtained:

$$\overline{C}_{\xi\eta} = C_{\xi\eta}^m + v_f\left(C_{\xi\alpha}^f - C_{\xi\alpha}^m\right)\left(\frac{\partial\overline{\varepsilon}_\alpha^f}{\partial\overline{\varepsilon}_\eta}\right) - v_f e_{\zeta\xi}^f\left(\frac{\partial\overline{E}_\zeta^f}{\partial\overline{\varepsilon}_\eta}\right) \quad \text{for } \overline{E}_\zeta = 0, \tag{15}$$

$$\overline{e}_{\ell\eta} = v_f\left(\in_{\ell\beta}^f - \in_{\ell\beta}^m\right)\left(\frac{\partial\overline{E}_\beta^f}{\partial\overline{\varepsilon}_\eta}\right) + v_f e_{\ell\xi}^f\left(\frac{\partial\overline{\varepsilon}_\xi^f}{\partial\overline{\varepsilon}_\eta}\right) \quad \text{for } \overline{E}_\zeta = 0, \tag{16}$$

$$\overline{\in}_{\ell\zeta} = \in_{\ell\zeta}^m + v_f\left(\in_{\ell\beta}^f - \in_{\ell\beta}^m\right)\left(\frac{\partial\overline{E}_\beta^f}{\partial\overline{E}_\zeta}\right) + v_f e_{\ell\eta}^f\left(\frac{\partial\overline{\varepsilon}_\eta^f}{\partial\overline{E}_\zeta}\right) \quad \text{for } \overline{\varepsilon}_\eta = 0. \tag{17}$$

It should be noted that the fiber-phase volume-average electric field ($\overline{E}_\zeta^f$) may have a nonzero value for a zero value of RVE volume-average electric field ($\overline{E}_\zeta = 0$) because of the electro-elastic coupling within the same (fiber) volume. This electro-elastic coupling may also cause a nonzero fiber-phase volume-average strain field ($\overline{\varepsilon}_\eta^f$) even though the RVE volume-average strain field ($\overline{\varepsilon}_\eta$) has zero value. So, the electro-elastic coupling terms ($\partial\overline{E}_\zeta^f/\partial\overline{\varepsilon}_\eta$, $\partial\overline{\varepsilon}_\eta^f/\partial\overline{E}_\zeta$) appear in the expressions [Eqs. (15)–(17)] of the effective electro-elastic constants.

It is clear from Eqs. (15)–(17) that the effective electro-elastic constants could be determined by computation of volume-average-field quantities for RVE and fiber phase and it is performed at present by the imposition of RVE volume-average strain and electric fields by means of homogeneous displacement and electric potential boundary conditions as discussed earlier within this section. However, for this computation, an electro-elastic analysis of RVE is to be carried out and this is done at present using a finite element (FE) procedure. The FE procedure is generally a very time-consuming and expensive procedure. But it may provide more realistic results in the prediction of electro-elastic constants of piezoelectric composites [44]. So, the FE procedure is utilized at present by the derivation of a three-dimensional FE model of RVE as presented in the next section. The solutions from the FE model of RVE for applied homogeneous kinematic boundary conditions yield the volume-average field quantities according to the following expressions:

$$\overline{\varepsilon}_\eta = \frac{1}{V_d}\left(\sum_{i=1}^{N_{V_d}}\int_{V_d^i}\varepsilon_\eta^i\mathrm{d}V_d^i\right), \overline{E}_\zeta = \frac{1}{V_d}\left(\sum_{i=1}^{N_{V_d}}\int_{V_d^i}E_\zeta^i\mathrm{d}V_d^i\right) \tag{18}$$

where N_{V_d} is the number of elements within a volume V_d (RVE/fiber phase/matrix phase); $\varepsilon_\eta^i/E_\zeta^i$ is a component of strain/electric field vector within the ith-element having the elemental volume of V_d^i. However, in the

determination of material constants, the volume-average strain and electric field quantities in RVE and fiber phase [Eq. (18)] are computed at present by choosing nine sets of homogeneous kinematic boundary conditions. The RVE is initially considered as a stress/strain/electric field free solid, and then, every set of boundary conditions over its boundary surfaces is applied separately. Every set of boundary conditions yields only one nonzero element of strain ($\overline{\varepsilon}_\eta$ at $\overline{E}_\zeta = 0$) or electric ($\overline{E}_\zeta$ at $\overline{\varepsilon}_\eta = 0$) field vector. Corresponding to such a nonzero element (say, $\langle \overline{\varepsilon}_\eta = \overline{\varepsilon}_1$ for $\eta =1$; $\overline{\varepsilon}_\eta = 0$ for $\eta = 2, 3, \ldots 6$; $\overline{E}_\zeta = 0 \rangle$ or $\langle \overline{E}_\zeta = \overline{E}_1$ for $\zeta =1$; $\overline{E}_\zeta = 0$ for $\zeta = 2, 3$; $\overline{\varepsilon}_\eta = 0 \rangle$), the gradient terms in Eqs. (15)–(17) could be written as

$$\frac{\partial \overline{\varepsilon}_\alpha^f}{\partial \overline{\varepsilon}_1} = \frac{\overline{\varepsilon}_\alpha^f}{\overline{\varepsilon}_1} \quad \text{for } \overline{E}_\zeta = 0, \tag{19}$$

$$\frac{\partial \overline{E}_\zeta^f}{\partial \overline{\varepsilon}_1} = \frac{\overline{E}_\zeta^f}{\overline{\varepsilon}_1} \quad \text{for } \overline{E}_\zeta = 0, \tag{20}$$

$$\frac{\partial \overline{\varepsilon}_\eta^f}{\partial \overline{E}_1} = \frac{\overline{\varepsilon}_\eta^f}{\overline{E}_1} \quad \text{for } \overline{\varepsilon}_\eta = 0, \tag{21}$$

$$\frac{\partial \overline{E}_\ell^f}{\partial \overline{E}_1} = \frac{\overline{E}_\ell^f}{\overline{E}_1} \quad \text{for } \overline{\varepsilon}_\eta = 0. \tag{22}$$

Introducing these terms in Eqs. (15)–(17), the effective constants, $\overline{C}_{\xi 1}$, $\overline{e}_{\ell 1}$ and $\overline{\in}_{\ell 1}$, can be obtained. A similar computation for all sets of boundary conditions yields all material constants. However, it is now important to consider the appropriate homogeneous electro-elastic kinematic boundary conditions for the computation of material constants, and these are given as follows. In specifying the boundary conditions, the displacements along r, θ and z directions are denoted by $u(r, \theta, z)$, $v(r, \theta, z)$ and $w(r, \theta, z)$, respectively, while the electric potential is denoted by $\phi(r, \theta, z)$.

(a) Effective constants ($\overline{C}_{\xi 1}$, $\overline{e}_{\ell 1}$):
   Boundary conditions: $u|_{-r} = 0$, $u|_{+r} = (\varepsilon_1^0 \times l_c)$, $v|_{\pm \theta} = 0$, $w|_{\pm z} = 0$, $\phi|_{\pm r, \pm \theta, \pm z} = 0$.
   Elements ($\overline{\varepsilon}_\eta$, $\overline{E}_\zeta$): $\overline{\varepsilon}_1 \approx \varepsilon_1^0$; $\overline{\varepsilon}_\eta = 0$ for $\eta = 2, 3, 4, 5, 6$; $\overline{E}_\zeta = 0$.
   Effective material constants:

$$\overline{C}_{\xi 1} = C_{\xi 1}^m + v_f \left(C_{\xi \alpha}^f - C_{\xi \alpha}^m \right) \left(\frac{\overline{\varepsilon}_\alpha^f}{\varepsilon_1^0} \right) - v_f e_{\zeta \xi}^f \left(\frac{\overline{E}_\zeta^f}{\varepsilon_1^0} \right),$$

$$\overline{e}_{\ell 1} = v_f \left(\in_{\ell \beta}^f - \in_{\ell \beta}^m \right) \left(\frac{\overline{E}_\beta^f}{\varepsilon_1^0} \right) + v_f e_{\ell \xi}^f \left(\frac{\overline{\varepsilon}_\xi^f}{\varepsilon_1^0} \right). \tag{23}$$

(b) Effective constants ($\overline{C}_{\xi 2}$, $\overline{e}_{\ell 2}$):
   Boundary conditions: $u|_{\pm r} = 0$, $v|_{-\theta} = 0$, $v|_{+\theta} = (\varepsilon_2^0 \times \theta_c)$, $w|_{\pm z} = 0$, $\phi|_{\pm r, \pm \theta, \pm z} = 0$.
   Elements ($\overline{\varepsilon}_\eta$, $\overline{E}_\zeta$): $\overline{\varepsilon}_2 \approx \varepsilon_2^0$; $\overline{\varepsilon}_\eta = 0$ for $\eta = 1, 3, 4, 5, 6$; $\overline{E}_\zeta = 0$.
   Effective material constants:

$$\overline{C}_{\xi 2} = C_{\xi 2}^m + v_f \left(C_{\xi \alpha}^f - C_{\xi \alpha}^m \right) \left(\frac{\overline{\varepsilon}_\alpha^f}{\varepsilon_2^0} \right) - v_f e_{\zeta \xi}^f \left(\frac{\overline{E}_\zeta^f}{\varepsilon_2^0} \right),$$

$$\overline{e}_{\ell 2} = v_f \left(\in_{\ell \beta}^f - \in_{\ell \beta}^m \right) \left(\frac{\overline{E}_\beta^f}{\varepsilon_2^0} \right) + v_f e_{\ell \xi}^f \left(\frac{\overline{\varepsilon}_\xi^f}{\varepsilon_2^0} \right). \tag{24}$$

(c) Effective constants ($\overline{C}_{\xi 3}$, $\overline{e}_{\ell 3}$):
   Boundary conditions: $u|_{\pm r} = 0$, $v|_{\pm \theta} = 0$, $w|_{-z} = 0$, $w|_{+z} = (\varepsilon_3^0 \times h_c)$, $\phi|_{\pm r, \pm \theta, \pm z} = 0$.
   Elements ($\overline{\varepsilon}_\eta$, $\overline{E}_\zeta$): $\overline{\varepsilon}_3 \approx \varepsilon_3^0$; $\overline{\varepsilon}_\eta = 0$ for $\eta = 1, 2, 4, 5, 6$; $\overline{E}_\zeta = 0$.

Effective material constants:

$$\overline{C}_{\xi 3} = C_{\xi 3}^m + v_f \left(C_{\xi\alpha}^f - C_{\xi\alpha}^m \right) \left(\frac{\overline{\varepsilon}_\alpha^f}{\varepsilon_3^0} \right) - v_f e_{\zeta\xi}^f \left(\frac{\overline{E}_\zeta^f}{\varepsilon_3^0} \right),$$

$$\overline{e}_{\ell 3} = v_f \left(\in_{\ell\beta}^f - \in_{\ell\beta}^m \right) \left(\frac{\overline{E}_\beta^f}{\varepsilon_3^0} \right) + v_f e_{\ell\xi}^f \left(\frac{\overline{\varepsilon}_\xi^f}{\varepsilon_3^0} \right). \tag{25}$$

(d) Effective constants $(\overline{C}_{\xi 4}, \overline{e}_{\ell 4})$:
Boundary conditions: $v|_{-z} = 0$, $v|_{+z} = 1/2 \, \varepsilon_4^0 \times h_c$, $w|_{-\theta} = 0$, $w|_{+\theta} = 1/2 \, \varepsilon_4^0 \times \theta_c$, $\phi|_{\pm r, \pm\theta, \pm z} = 0$.
Elements $(\overline{\varepsilon}_\eta, \overline{E}_\zeta)$: $\overline{\varepsilon}_4 \approx \varepsilon_4^0$; $\overline{\varepsilon}_\eta = 0$ for $\eta = 1, 2, 3, 5, 6$; $\overline{E}_\zeta = 0$.
Effective material constants:

$$\overline{C}_{\xi 4} = C_{\xi 4}^m + v_f \left(C_{\xi\alpha}^f - C_{\xi\alpha}^m \right) \left(\frac{\overline{\varepsilon}_\alpha^f}{\varepsilon_4^0} \right) - v_f e_{\zeta\xi}^f \left(\frac{\overline{E}_\zeta^f}{\varepsilon_4^0} \right),$$

$$\overline{e}_{\ell 4} = v_f \left(\in_{\ell\beta}^f - \in_{\ell\beta}^m \right) \left(\frac{\overline{E}_\beta^f}{\varepsilon_4^0} \right) + v_f e_{\ell\xi}^f \left(\frac{\overline{\varepsilon}_\xi^f}{\varepsilon_4^0} \right). \tag{26}$$

(e) Effective constants $(\overline{C}_{\xi 5}, \overline{e}_{\ell 5})$:
Boundary conditions: $u|_{-z} = 0$, $u|_{+z} = 1/2 \, \varepsilon_5^0 \times h_c$, $w|_{-r} = 0$, $w|_{+r} = 1/2 \, \varepsilon_5^0 \times l_c$, $\phi|_{\pm r, \pm\theta, \pm z} = 0$.
Elements $(\overline{\varepsilon}_\eta, \overline{E}_\zeta)$: $\overline{\varepsilon}_5 \approx \varepsilon_5^0$; $\overline{\varepsilon}_\eta = 0$ for $\eta = 1, 2, 3, 4, 6$; $\overline{E}_\zeta = 0$.
Effective material constants:

$$\overline{C}_{\xi 5} = C_{\xi 5}^m + v_f \left(C_{\xi\alpha}^f - C_{\xi\alpha}^m \right) \left(\frac{\overline{\varepsilon}_\alpha^f}{\varepsilon_5^0} \right) - v_f e_{\zeta\xi}^f \left(\frac{\overline{E}_\zeta^f}{\varepsilon_5^0} \right),$$

$$\overline{e}_{\ell 5} = v_f \left(\in_{\ell\beta}^f - \in_{\ell\beta}^m \right) \left(\frac{\overline{E}_\beta^f}{\varepsilon_5^0} \right) + v_f e_{\ell\xi}^f \left(\frac{\overline{\varepsilon}_\xi^f}{\varepsilon_5^0} \right). \tag{27}$$

(f) Effective constants $(\overline{C}_{\xi 6}, \overline{e}_{\ell 6})$:
Boundary conditions: $u|_{-\theta} = 0$, $u|_{+\theta} = 1/2 \, \varepsilon_6^0 \times \theta_c$, $v|_{-r} = 0$, $v|_{+r} = 1/2 \, \varepsilon_6^0 \times l_c$, $\phi|_{\pm r, \pm\theta, \pm z} = 0$.
Elements $(\overline{\varepsilon}_\eta, \overline{E}_\zeta)$: $\overline{\varepsilon}_6 \approx \varepsilon_6^0$; $\overline{\varepsilon}_\eta = 0$ for $\eta = 1, 2, 3, 4, 5$; $\overline{E}_\zeta = 0$.
Effective material constants:

$$\overline{C}_{\xi 6} = C_{\xi 6}^m + v_f \left(C_{\xi\alpha}^f - C_{\xi\alpha}^m \right) \left(\frac{\overline{\varepsilon}_\alpha^f}{\varepsilon_6^0} \right) - v_f e_{\zeta\xi}^f \left(\frac{\overline{E}_\zeta^f}{\varepsilon_6^0} \right),$$

$$\overline{e}_{\ell 6} = v_f \left(\in_{\ell\beta}^f - \in_{\ell\beta}^m \right) \left(\frac{\overline{E}_\beta^f}{\varepsilon_6^0} \right) + v_f e_{\ell\xi}^f \left(\frac{\overline{\varepsilon}_\xi^f}{\varepsilon_6^0} \right). \tag{28}$$

(g) Effective constant $(\overline{\in}_{\ell 1})$:
Boundary conditions: $\phi|_{\pm z} = 0$, $\phi|_{\pm\theta} = 0$, $\phi|_{-r} = 0$, $\phi|_{+r} = -(E_1^0 \times l_c)$, $u|_{\pm r} = 0$, $v|_{\pm\theta} = 0$, $w|_{\pm z} = 0$.
Elements $(\overline{\varepsilon}_\eta, \overline{E}_\zeta)$: $\overline{E}_1 \approx E_1^0$; $\overline{E}_\zeta = 0$ for $\zeta = 2, 3$; $\overline{\varepsilon}_\eta = 0$.

Effective material constants:

$$\overline{\in}_{\ell 1} = \in_{\ell 1}^m + v_f \left(\in_{\ell \beta}^f - \in_{\ell \beta}^m \right) \left(\frac{\overline{E}_\beta^f}{E_1^0} \right) + v_f e_{\ell \eta}^f \left(\frac{\overline{\varepsilon}_\eta^f}{E_1^0} \right). \tag{29}$$

(h) Effective constant ($\overline{\in}_{\ell 2}$):
   Boundary conditions: $\phi|_{\pm r} = 0$, $\phi|_{\pm z} = 0$, $\phi|_{-\theta} = 0$, $\phi|_{+\theta} = -(E_2^0 \times \theta_c)$, $u|_{\pm r} = 0$, $v|_{\pm \theta} = 0$, $w|_{\pm z} = 0$.
   Elements ($\overline{\varepsilon}_\eta$, $\overline{E}_\zeta$): $\overline{E}_2 \approx E_2^0$; $\overline{E}_\zeta = 0$ for $\zeta = 1, 3$; $\overline{\varepsilon}_\eta = 0$.
   Effective material constants:

$$\overline{\in}_{\ell 2} = \in_{\ell 2}^m + v_f \left(\in_{\ell \beta}^f - \in_{\ell \beta}^m \right) \left(\frac{\overline{E}_\beta^f}{E_2^0} \right) + v_f e_{\ell \eta}^f \left(\frac{\overline{\varepsilon}_\eta^f}{E_2^0} \right). \tag{30}$$

(i) Effective constant ($\overline{\in}_{\ell 3}$):
   Boundary conditions: $\phi|_{\pm r} = 0$, $\phi|_{\pm \theta} = 0$, $\phi|_{-z} = 0$, $\phi|_{+z} = -(E_3^0 \times h_c)$, $u|_{\pm r} = 0$, $v|_{\pm \theta} = 0$, $w|_{\pm z} = 0$.
   Elements ($\overline{\varepsilon}_\eta$, $\overline{E}_\zeta$): $\overline{E}_3 \approx E_3^0$; $\overline{E}_\zeta = 0$ for $\zeta = 1, 2$; $\overline{\varepsilon}_\eta = 0$.
   Effective material constants:

$$\overline{\in}_{\ell 3} = \in_{\ell 3}^m + v_f \left(\in_{\ell \beta}^f - \in_{\ell \beta}^m \right) \left(\frac{\overline{E}_\beta^f}{E_3^0} \right) + v_f e_{\ell \eta}^f \left(\frac{\overline{\varepsilon}_\eta^f}{E_3^0} \right). \tag{31}$$

4 FE model of RVE

The constitutive relations for fiber and matrix phases within the RVE can be expressed as

$$\left\{ \begin{array}{c} \boldsymbol{\sigma}^q \\ \boldsymbol{D}^q \end{array} \right\} = \boldsymbol{C}^q \left\{ \begin{array}{c} +\boldsymbol{\varepsilon} \\ -\boldsymbol{E} \end{array} \right\}. \tag{32}$$

The superscript q in Eq. (32) denotes the quantities within the fiber or the matrix phase volume according to its value as 1 or 2, respectively. The different matrix and vector quantities in Eq. (32) are as follows:

$$\left\{ \begin{array}{c} +\boldsymbol{\varepsilon} \\ -\boldsymbol{E} \end{array} \right\} = \left\{ \varepsilon_1 \ \varepsilon_2 \ \varepsilon_3 \ \varepsilon_4 \ \varepsilon_5 \ \varepsilon_6 \ -E_1 \ -E_2 \ -E_3 \right\}^{\mathrm{T}},$$

$$\left\{ \begin{array}{c} \boldsymbol{\sigma} \\ \boldsymbol{D} \end{array} \right\} = \left\{ \sigma_1 \ \sigma_2 \ \sigma_3 \ \sigma_4 \ \sigma_5 \ \sigma_6 \ D_1 \ D_2 \ D_3 \right\}^{\mathrm{T}},$$

$$\boldsymbol{C}^1 = \left[\begin{array}{cc} \boldsymbol{C}_f & \boldsymbol{e}_f^{\mathrm{T}} \\ \boldsymbol{e}_f & -\boldsymbol{\in}_f \end{array} \right], \boldsymbol{C}^2 = \left[\begin{array}{cc} \boldsymbol{C}_m & \boldsymbol{0} \\ \boldsymbol{0} & -\boldsymbol{\in}_m \end{array} \right] \tag{33}$$

where $\boldsymbol{C}_f/\boldsymbol{C}_m$ is the stiffness matrix for the fiber/matrix phase; $\boldsymbol{\in}_f$ / $\boldsymbol{\in}_m$ is the permittivity matrix of the fiber/matrix phase; $\boldsymbol{e}_f$ is the piezoelectric matrix of the fiber phase. The form of these property matrices is given in Eq. (A.1). It should be noted that Eq. (A.1) represents the material properties for longitudinally (radial direction) poled piezoelectric fibers. The electro-elastic state at any point within the RVE can be defined by an electro-elastic state vector ($\boldsymbol{d}$) as

$$\boldsymbol{d} = \left[u \ v \ w \ \phi \right]^{\mathrm{T}}. \tag{34}$$

Using this electro-elastic state vector ($\boldsymbol{d}$), the strain ($\boldsymbol{\varepsilon}$) and electric ($\boldsymbol{E}$) field vectors at any point within the RVE can be expressed in terms of an operator matrix ($\boldsymbol{L}$) as

$$\left\{ \begin{array}{c} +\boldsymbol{\varepsilon} \\ -\boldsymbol{E} \end{array} \right\} = \boldsymbol{L}\boldsymbol{d}. \tag{35}$$

The form of the operator matrix (L) is given in Eq. (A.2). Using Eq. (32), the first variation of the electro-elastic internal energy of RVE can be written as [45]

$$\delta U = \sum_{q=1}^{2} \left(\int_{V^q} \left\langle \lfloor \delta \boldsymbol{\varepsilon} \ -\delta \boldsymbol{E} \rfloor \, \boldsymbol{C}^q \left\{ \begin{array}{c} +\boldsymbol{\varepsilon} \\ -\boldsymbol{E} \end{array} \right\} \right\rangle \mathrm{d}V^q \right) \tag{36}$$

where δ is an operator for the first variation; V^q is the volume of the fiber phase ($q = 1$) or matrix phase ($q = 2$); introducing Eq. (35) in Eq. (36), the following form of δU can be obtained:

$$\delta U = \sum_{q=1}^{2} \left(\int_{V^q} \left\langle \delta \boldsymbol{d}^{\mathrm{T}} \boldsymbol{L}^{\mathrm{T}} \boldsymbol{C}^q \boldsymbol{L} \boldsymbol{d} \right\rangle \mathrm{d}V^q \right). \tag{37}$$

For deriving the finite element model, the volume of the RVE is discretized by 27-node isoparametric hexahedral elements. At any point within a typical elements, the electro-elastic state vector ($\boldsymbol{d}$) can be written as

$$\boldsymbol{d} = \boldsymbol{N} \boldsymbol{d}^e \tag{38}$$

where $\boldsymbol{N}$ is the shape function matrix and $\boldsymbol{d}^e$ is the elemental nodal electro-elastic state vector. Introducing Eq. (38) in Eq. (37), the simplified expression for the first variation of the electro-elastic internal energy (δU^e) of a typical element can be obtained as

$$\delta U^e = (\delta \boldsymbol{d}^e)^{\mathrm{T}} \left\langle \boldsymbol{K}^e \boldsymbol{d}^e \right\rangle$$
$$\boldsymbol{K}^e = \int_{V_e^q} \left(\boldsymbol{N}^{\mathrm{T}} \boldsymbol{L}^{\mathrm{T}} \boldsymbol{C}^q \boldsymbol{L} \boldsymbol{N} \right) \mathrm{d}V_e^q \tag{39}$$

where V_e^q is the elemental volume within the fiber phase ($q = 1$) or matrix phase ($q = 2$). Assembling the elemental equations [Eq. (39)] in the global space, the global expression for the internal energy of an RVE can be obtained as

$$\delta U = (\delta \boldsymbol{X})^{\mathrm{T}} \langle \boldsymbol{K} \boldsymbol{X} \rangle \tag{40}$$

where $\boldsymbol{K}$ is the global electro-elastic coefficient matrix; $\boldsymbol{X}$ is the global nodal electro-elastic state vector. The present electro-elastic FE analysis of RVE is due to the applied kinematic boundary conditions [Eqs. (23)–(31)] over its (RVE) boundary surfaces. If these boundary conditions are directly applied to the boundary surfaces of RVE, then it results in over-constrained RVE edges [44]. This kind of over-constrained deformation of RVE could be avoided by applying the kinematic boundary conditions over the full FE model of RVE instead of applying the same directly to the RVE boundary surfaces [44]. So, the kinematic boundary conditions [Eqs. (23)–(31)] are presently applied over the FE model of RVE [Eq. (40)] following a procedure described in [46]. For a specified nodal electric potential or displacement over the boundary surface, the first variation of the corresponding element of $\boldsymbol{X}$ (say, X_i) is zero ($\delta X_i = 0$). Thus, the corresponding (i^{th}) row of $\boldsymbol{K}$ is to be deleted, while a column ($\boldsymbol{P}_i$) of $\boldsymbol{K}$ with the same index (i) is to be removed for the formation of the electric potential or displacement–load vector as

$$\delta U = (\delta \boldsymbol{X}_r)^{\mathrm{T}} \langle \boldsymbol{K}_r \boldsymbol{X}_r + \boldsymbol{P}_i X_i \rangle \tag{41}$$

where $\boldsymbol{K}_r$ and $\boldsymbol{X}_r$ are the reduced electro-elastic coefficient matrix and nodal electro-elastic state vector, respectively. For a number (N_b) of specified values of nodal degrees of freedoms over the boundary surfaces of RVE, Eq. (41) can be written in general form as

$$\delta U = (\delta \boldsymbol{X}_r)^{\mathrm{T}} \left\langle \boldsymbol{K}_r \boldsymbol{X}_r + \sum_{i=1}^{N_b} \boldsymbol{P}_i X_i \right\rangle. \tag{42}$$

Employing the principle of minimum potential energy, Eq. (42) can be written as follows:

$$\boldsymbol{K}_r \boldsymbol{X}_r = - \sum_{i=1}^{N_b} \boldsymbol{P}_i X_i. \tag{43}$$

Equation (43) represents the electro-elastic finite element model of RVE under the specified nodal values of electric potential and/or displacement. Using Eq. (43), the nodal solutions for electric potential and displacement fields within the RVE corresponding to every set of boundary conditions [Eqs. (23)–(31)] can be obtained. Subsequently, the volume-average (RVE/phase) strain and electric fields can be computed according to Eq. (18) using these nodal solutions.

5 Arrangement of electrodes

The present cylindrically orthotropic piezoelectric composite is designed to utilize it as a material of distributed actuator in control of the vibration of plane structures of revolution. So, the electrodes are to be provided over its boundary surfaces in order to activate it by supplying external voltage. The external voltage induces an electric field within the smart composite resulting in necessary control activity. According to the geometrical construction and poling direction of the present smart composite, the magnitude of one effective piezoelectric coefficient (e_{11}, 1 for radial direction) is significantly larger than the magnitudes of other effective piezoelectric coefficients. Thus, this effective coefficient (e_{11}) is utilized for its (smart composite) better control performance, and it could be achieved by applying the electric field in the radial direction by an arrangement of electrodes over the top and bottom surfaces of the composite layer as illustrated in Fig. 2a. Figure 2a shows the top/bottom surface of the SPFRC layer over which a surface electrode is provided at the radial gap of any two consecutive short fibers. The uniform polarity of external voltage is considered for the top and bottom surface electrodes lying on the same radial location, while any two consecutive electrodes along the radial direction are of opposite polarity. Any two consecutive electrodes of opposite polarity are denoted as a pair of electrodes. Across all pairs of electrodes, a uniform value of applied voltage is considered that yields uniform magnitude of the electric the field within all such pairs. But the radial component of the electric field within a pair of electrodes is in opposite direction to that of the same within the consecutive pairs of electrodes. For obtaining the electrically
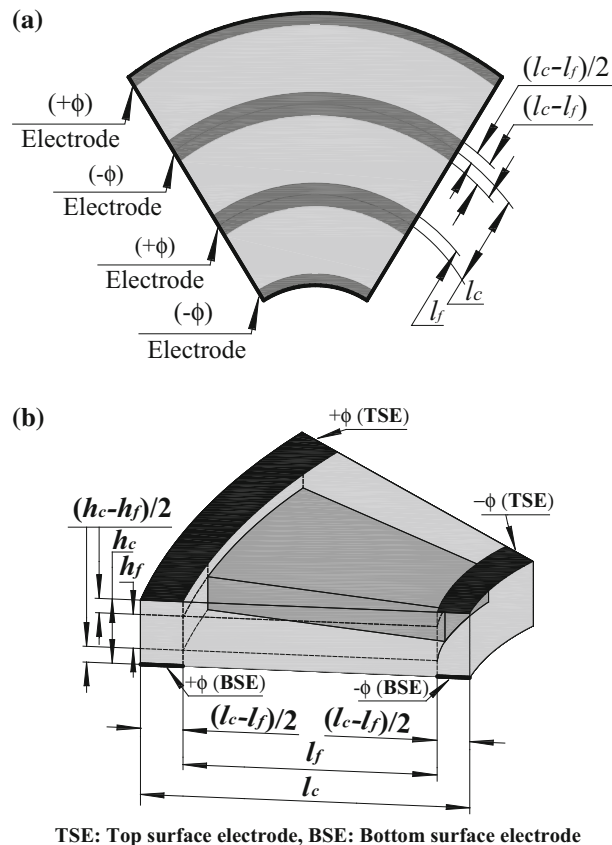

TSE: Top surface electrode, BSE: Bottom surface electrode

Fig. 2 a *Top/bottom* surface of the cylindrically orthotropic piezoelectric composite with electrodes, **b** the RVE with electrode surfaces

induced actuation force in the same direction from all pairs of electrodes, the corresponding piezoelectric fibers are poled along the radial direction in alternate manner. However, according to the present arrangements of surface electrodes and short piezoelectric fibers, the macroscopic behavior of the smart composite actuator can be estimated by defining an elemental volume as illustrated in Fig. 2b that is basically a volume of RVE with surface electrodes.

In this arrangement, it seems a too small radial gap between any two consecutive surface electrodes. But this facilitates to achieve a significant magnitude of externally induced electric field in expense of small applied voltage across the pairs of surface electrodes. The difficulty may arise in the fabrication of electrodes because of the small gap between any two consecutive electrodes, but this gap can be increased by increasing the length of the fibers in terms of the increase in fiber aspect ratio. The fiber aspect ratio does not have much effect on the magnitude of the effective coefficient (e_{11}) as it is shown in a later section (Sect. 7.1). So, the aforesaid difficulty may be mitigated considering higher fiber aspect ratio. In this case (higher aspect ratio), the only change would be the requirement of more external voltage for the same magnitude of the applied electric field.

It is now required to determine the magnitude of the induced electric field for an applied voltage across the pairs of electrodes in order to use the smart composite as an actuator. In this evaluation of the induced electric field, the difficulty arises due to the material heterogeneity. The effective properties or constitutive behavior of the smart composite is valid only for specially statistically homogeneous fields, which could be produced by means of homogeneous kinematic/kinetic boundary conditions over the surface of a large composite [42]. The present applied electric potentials over the surface electrodes do not satisfy the conditions for homogeneous kinematic boundary conditions. So, in a strict sense, the corresponding statistically homogeneous electric field would not be adequate to the effective constitutive relation. As a consequence, for a situation where the aforesaid specially statistically homogeneous fields do not arise or could not be produced, an assumption of local averages of fields over the volume of an RVE may be made to salvage the analysis [42]. Following this assumption in the present analysis, the local electric field within the elemental volume (RVE) with surface electrodes (Fig. 2b) is considered as local volume-average electric field over the same volume (RVE). Without this assumption in the present analysis, it is difficult to model the induced electric field within a local heterogeneous volume of the large smart composite actuator. However, as per this consideration, the induced electric field due to an external voltage could be taken as its volume-average quantity over the volume of the RVE according to Eq. (12). Now, for structural applications of the smart actuator under the assumption of small strain, the induced electric field due to strain of overall structure is of negligibly small magnitude as compared to the large magnitude of the applied electric field by means of external voltage. So, the magnitude of an RVE volume-average electric field ($\overline{E}$) may be considered as a function of applied voltage (V) only. Since one value of applied voltage yields one magnitude of $\overline{E}$ within the actuator, $\overline{E}$ is a single-valued function of applied voltage (V). This functional relation may be represented by the following expressions [Eq. (44)], in which $G_r(V)$, $G_\theta(V)$ and $G_z(V)$ are the functions of applied voltage corresponding to the components of the volume-average electric field ($\overline{E}_r, \overline{E}_\theta, \overline{E}_z$):

$$\overline{E}_r = G_r(V)\,V, \overline{E}_\theta = G_\theta(V)\,V, \overline{E}_z = G_z(V)\,V. \tag{44}$$

The forgoing demonstration is for a layer of present SPFRC actuator comprised of one layer of short piezo-electric fibers. Similar SPFRC layers can be stacked with proper alignment of electrode polarities to form a lamina of SPFRC actuator as illustrated in Fig. 3. The electrodes of the same polarity of this smart actuator lamina are vertically coincident, and their (electrodes) ends are exposed on the circumferential edge surfaces ($+\theta$ and $-\theta$ surfaces) of the lamina. So, the external voltage can be provided through these exposed ends of electrodes.

6 FE model of a smart annular plate

The present cylindrically orthotropic SPFRC actuator is designed mainly for controlling the vibration of plane structures of revolution. In order to substantiate this objective, a vibration analysis of an annular plate integrated with the patches of the present SPFRC actuator is performed by deriving a close-loop FE model of the overall smart annular plate. Figure 4 shows a substrate annular plate integrated with four identical patches of a presently designed cylindrically orthotropic SPFRC actuator. The middle plane of the substrate annular plate is considered as the reference plane, and the origin of the reference cylindrical coordinate system (r, θ, z) is located at the center of this reference annular plane. The inner and outer radii of the overall plate are denoted by r_i and r_o, respectively. The thickness of the substrate plate and actuator patches are symbolized by h and h_p, respectively. The circumferential span of every patch is denoted by β^o, and their locations on the top
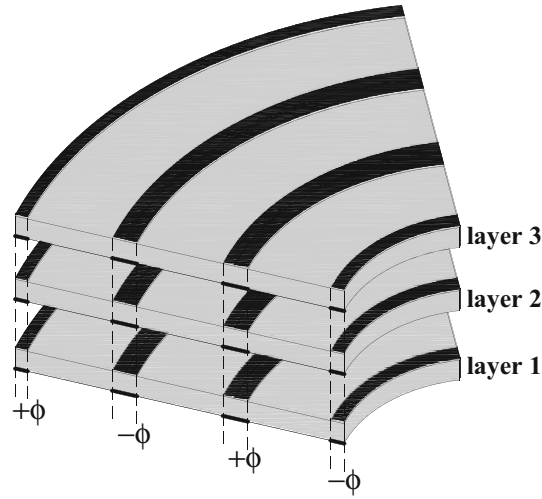
Fig. 3 Stack of cylindrically orthotropic SPFRC layers in forming a lamina
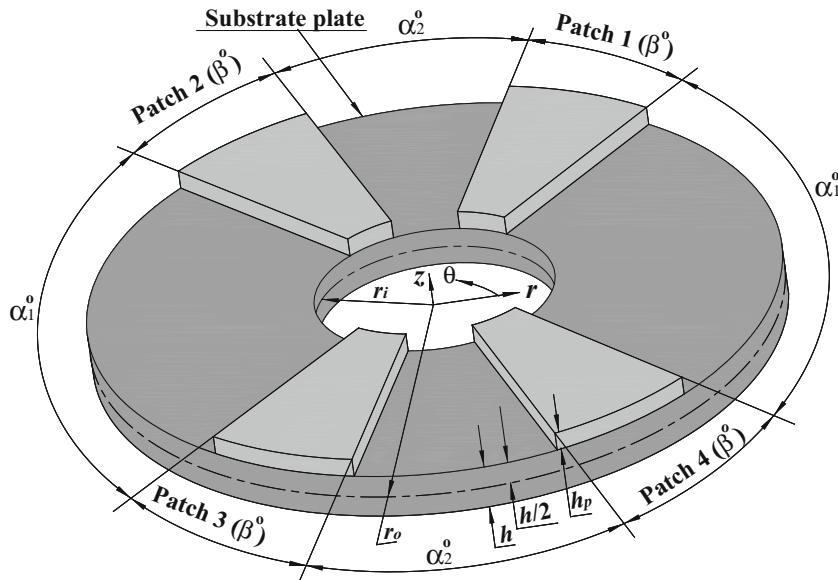

Fig. 4 Schematic diagram of an annular plate integrated with the patches of cylindrically orthotropic PFRC actuators

surface of the substrate plate are indicated by the angles α_1^o and α_2^o (Fig. 4). The radial length of the patches is identical to that of the substrate annular plate, and the patches are considered to be located symmetrically ($\alpha_1^o = \alpha_1^o = \alpha^o$). The fibers within the actuator patches are aligned in the plane of the plate and oriented along the radial direction. The state of stress and the state of strain at any point in the overall annular plate can be written as

$$\boldsymbol{\sigma}_b = [\sigma_r \ \ \sigma_\theta \ \ \tau_{r\theta}]^{\mathrm{T}}, \boldsymbol{\sigma}_s = \begin{bmatrix} \tau_{rz} & \tau_{\theta z} \end{bmatrix}^{\mathrm{T}}, \tag{45}$$

$$\boldsymbol{\varepsilon}_b = [\varepsilon_r \ \ \varepsilon_\theta \ \ \varepsilon_{r\theta}]^{\mathrm{T}}, \boldsymbol{\varepsilon}_s = \begin{bmatrix} \varepsilon_{rz} & \varepsilon_{\theta z} \end{bmatrix}^{\mathrm{T}}. \tag{46}$$

Since a thin overall annular plate is considered in the present study, its kinematics of deformation is defined according to the first-order shear deformation theory (FSDT) as follows:

$$u_p (r, \theta, z, t) = u_0 (r, \theta, t) + z\phi_r (r, \theta, t), \tag{47.1}$$

$$v_p (r, \theta, z, t) = v_0 (r, \theta, t) + z\phi_\theta (r, \theta, t), \tag{47.2}$$

$$w_p (r, \theta, z, t) = w_0 (r, \theta, t). \tag{47.3}$$

The generalized displacements in Eqs. (47.1)–(47.3) can be represented by a displacement vector (d_p) as follows:

$$d_p = \{ u_o \; v_o \; w_o \; \phi_r \; \phi_\theta \}^{\mathrm{T}}, \tag{48}$$

According to this displacement field [Eq. (47)], the linear strain-displacement relations at any point of the overall annular plate can be written in terms of the operator matrices (L_{bt}, L_{br}, L_s) as

$$\varepsilon_b = (L_{bt} + zL_{br})\,d_p, \; \varepsilon_s = L_s d_p. \tag{49}$$

In Eq. (49), the forms of operator matrices are given in Eqs. (A.3)–(A.5). The constitutive relations for the substrate isotropic annular plate can be written as

$$\sigma_b^k = C_b^k \varepsilon_b \,, \sigma_s^k = C_s^k \varepsilon_s, \quad k = 1 \tag{50}$$

where C_b^k and $C_s^k (k = 1)$ are the stiffness matrices for the isotropic material of substrate plate. The forms of these stiffness matrices are given in Eq. (A.6) in which the symbols E and ν stand for Young's modulus and Poisson's ratio, respectively. The constitutive relations for the cylindrically orthotropic piezoelectric composite can be written as

$$\sigma_b^k = C_b^k \varepsilon_b - e_b E, \quad \sigma_s^k = C_s^k \varepsilon_s - e_s E, \quad D = e_b^{\mathrm{T}} \varepsilon_b + e_s^{\mathrm{T}} \varepsilon_s + \in E, \quad k = 2. \tag{51}$$

In Eqs. (50) and (51), the superscript k denotes the substrate plate or the actuator patch according to its value as 1 or 2, respectively. The forms of elastic matrices (C_b^k, C_s^k, $k = 2$), piezoelectric matrices (e_b, e_s) and permittivity matrix ($\in$) appearing in Eq. (51) are given in Eqs. (A.7)–(A.9). The present analysis deals with the small amplitude vibration of the overall smart annular plate with an assumption of small strain. Under the small strain of overall smart annular plate and uniform value of applied voltage (V) across all pairs of surface electrodes, the components (E_r, E_θ, E_z) of the volume-average electric field (E) within the actuator patch may be assumed as functions of applied voltage (V) only as it is discussed in the previous section [Eq. (44)]. The electric field (E) then can be written as

$$E = \begin{bmatrix} G_r(V) \; G_\theta(V) \; G_z(V) \end{bmatrix}^{\mathrm{T}} V. \tag{52}$$

The overall annular plate is considered to be subjected to a distributed transverse harmonic load ($p(r, \theta, t)$). Thus, the first variations of total potential energy (δT_p) and total kinetic energy (δT_k) of the overall smart annular plate at an instant of time (t) can be written as

$$\delta T_p = \int_{r_i}^{r_o} \int_0^{2\pi} \left[\sum_{k=1}^{2} \int_{h_k}^{h_{k+1}} \left(\delta \varepsilon_b^{\mathrm{T}} \sigma_b^k + \delta \varepsilon_s^{\mathrm{T}} \sigma_s^k \right) \mathrm{d}z - \int_{h_k}^{h_{k+1}} (\delta E^{\mathrm{T}} D)_{k=2} \mathrm{d}z - \delta w_p \; \langle p(r, \theta, t) \rangle_{z=-h/2} \right] r \mathrm{d}\theta \mathrm{d}r, \tag{53}$$

$$\delta T_k = \int_{r_i}^{r_o} \int_0^{2\pi} \left(\sum_{k=1}^{2} \int_{h_k}^{h_{k+1}} \left(\{ \delta \dot{u}_p \; \delta \dot{v}_p \; \delta \dot{w}_p \} \rho^k \{ \dot{u}_p \; \dot{v}_p \; \dot{w}_p \}^{\mathrm{T}} \right) \mathrm{d}z \right) r \mathrm{d}\theta \mathrm{d}r \tag{54}$$

where ρ^k is the mass density of the substrate plate ($k = 1$) or actuator patch ($k = 2$). Substituting Eqs. (50), (51), (49) and (48) in Eqs. (53)–(54), the first variations of the total potential energy and total kinetic energy of the overall smart annular plate can be written as

$$\delta T_p = \int_{r_i}^{r_0} \int_0^{2\pi} \delta d_p^{\mathrm{T}} \left[\begin{array}{l} \langle L_{bt}^{\mathrm{T}} A_b L_{bt} + L_{bt}^{\mathrm{T}} B_b L_{br} + L_{br}^{\mathrm{T}} B_b L_{bt} + L_{br}^{\mathrm{T}} D_b L_{br} + L_s^{\mathrm{T}} A_s L_s \rangle d_p \\ - \langle L_{bt}^{\mathrm{T}} A_{be}(V) + L_{br}^{\mathrm{T}} B_e(V) + L_s^{\mathrm{T}} A_{se}(V) \rangle V - P_{\mathrm{cm}}(t) \end{array} \right] r \mathrm{d}\theta \mathrm{d}r, \tag{55}$$

$$\delta T_k = \int_{r_i}^{r_o} \int_0^{2\pi} \left(\delta \dot{d}_p^{\mathrm{T}} \overline{m} \dot{d}_p \right) r \mathrm{d}\theta \mathrm{d}r. \tag{56}$$

In Eqs. (55)–(56), the rigidity matrices (A_b, A_s, B_b, D_b), electro-elastic coupling vectors ($A_{be}(V)$, $A_{se}(V)$, $B_e(V)$), mass matrix per unit area ($\overline{m}$) and load vector ($P_{cm}(t)$) are given by

$$A_b = \sum_{k=1}^{2} \int_{h_k}^{h_{k+1}} C_b^k dz, \quad A_s = \sum_{k=1}^{2} \int_{h_k}^{h_{k+1}} C_s^k dz, \quad B_b = \sum_{k=1}^{2} \int_{h_k}^{h_{k+1}} C_b^k z dz, \quad D_b = \sum_{k=1}^{2} \int_{h_k}^{h_{k+1}} C_b^k z^2 dz,$$

$$A_{be}(V) = \int_{h_k}^{h_{k+1}} e_b \{G_r(V)G_\theta(V)G_z(V)\}^{\mathrm{T}}\big|_{k=2} dz, A_{se}(V) = \int_{h_k}^{h_{k+1}} e_s \{G_r(V)G_\theta(V)G_z(V)\}^{\mathrm{T}}\big|_{k=2} dz,$$

$$B_e(V) = \int_{h_k}^{h_{k+1}} e_b \{G_r(V)G_\theta(V)G_z(V)\}^{\mathrm{T}}\big|_{k=2} z dz, \quad P_{cm}(t) = \left\{0\ 0\ p(r,\theta,t)\ 0\ 0\right\}^{\mathrm{T}},$$

$$\overline{m} = \sum_{k=1}^{2} \int_{h_k}^{h_{k+1}} \left(Z_t^{\mathrm{T}} \rho^k Z_t + Z_t^{\mathrm{T}} \rho^k Z_r + Z_r^{\mathrm{T}} \rho^k Z_t + Z_r^{\mathrm{T}} \rho^k Z_r\right) dz. \tag{57}$$

The co-ordinate matrices (Z_t, Z_r) appearing in Eq. (57) are given in Eq. (A.10). For an element without actuator patch, the electro-elastic coupling vectors ($A_{be}(V)$, $A_{se}(V)$, $B_e(V)$) are null vectors. Also, the rigidity matrices (A_b, A_s, B_b, D_b) and mass matrix ($\overline{m}$) are only for the substrate plate ($k = 1$). For deriving the FE model of the overall annular plate, the plane of the plate is discretized into ($n_1 \times m_1$) number of 9-node isoparametric elements. The equally spaced circumferential lines divide the radial length ($r_0 - r_i$) into n_1 number of equal divisions, while the equally spaced radial lines divide the circumference (2π) into m_1 number of equal divisions. The inner/outer boundaries of a typical element along the radial and circumferential directions are denoted by r_i^e/r_o^e and θ_i^e/θ_o^e, respectively. The generalized displacement vector [Eq. (48)] within an element can be written as

$$d_p = N_p d_p^e \tag{58}$$

where N_p is the shape function matrix and d_p^e is the elemental nodal displacement vector. Using Eq. (58), the total strain energy [Eq. (55)] and the total kinetic energy [Eq. (56)] for a typical element can be expressed as

$$\delta T_p^e = (\delta d_p^e)^{\mathrm{T}} \left\langle (K_b^e + K_s^e) d_p^e - P_E^e(V) V - P_M^e(t) \right\rangle, \tag{59}$$

$$\delta T_k^e = (\delta \dot{d}_p^e)^{\mathrm{T}} M^e \dot{d}_p^e. \tag{60}$$

In Eqs. (59)–(60), the different matrix quantities are as follows:

$$K_b^e = \int_{r_i^e}^{r_o^e} \int_{\theta_i^e}^{\theta_o^e} \left[N_p^{\mathrm{T}}(L_{bt}^{\mathrm{T}} A_b L_{bt} + L_{bt}^{\mathrm{T}} B_b L_{br} + L_{br}^{\mathrm{T}} B_b L_{bt} + L_{br}^{\mathrm{T}} D_b L_{br})N_p\right] r d\theta dr,$$

$$K_s^e = \int_{r_i^e}^{r_o^e} \int_{\theta_i^e}^{\theta_o^e} \left[N_p^{\mathrm{T}}(L_s^{\mathrm{T}} A_s L_s)N_p\right] r d\theta dr,$$

$$P_E^e(V) = \int_{r_i^e}^{r_o^e} \int_{\theta_i^e}^{\theta_o^e} \left[N_p^{\mathrm{T}} \langle L_{bt}^{\mathrm{T}} A_{be}(V) + L_{br}^{\mathrm{T}} B_e(V) + L_s^{\mathrm{T}} A_{se}(V)\rangle\right] r d\theta dr,$$

$$P_M^e(t) = \int_{r_i^e}^{r_o^e} \int_{\theta_i^e}^{\theta_o^e} \left[N_p^{\mathrm{T}} P_{cm}(t)\right] r d\theta dr,$$

$$M^e = \int_{r_i^e}^{r_o^e} \int_{\theta_i^e}^{\theta_o^e} \left[N_p^{\mathrm{T}} \overline{m} N_p\right] r d\theta dr. \tag{61}$$

In Eq. (61), the bending and shear counterparts of the total stiffness matrix are separately formulated for implementing the selective integration in a straight forward manner. The governing equations of motion of the overall smart annular plate are derived employing Hamilton's principle as

$$\int_{t_1}^{t_2} \left(\delta T_k^e - \delta T_p^e\right) dt = 0. \tag{62}$$

Introducing the expressions of δT_p^e and δT_k^e [Eqs. (59)–(60)] in Eq. (62), the following governing equations of motion for a typical element of the overall smart annular plate can be obtained:

$$M^e \ddot{d}_p^e + (K_b^e + K_s^e)d_p^e = P_E^e(V)V + P_M^e(t). \tag{63}$$

Assembling the elemental governing equations of motion [Eq. (63)] into the global space, the following global equations of motion of the overall smart annular plate can be obtained:

$$M\ddot{X}_p + (K_b + K_s)X_p = \sum_{q=1}^{4} P_E^q(V^q)V^q + P_M(t). \tag{64}$$

In Eq. (64), M is the global mass matrix; K_b and K_s are bending and shear counterparts of the global stiffness matrix; $P_M(t)$ is the global mechanical load vector; X_p is the global nodal displacement vector; P_E^q is the coefficient vector of the global electrical load for the qth actuator patch; and V^q is the applied voltage to the qth actuator patch.

6.1 Smart damping

The external voltage to the actuator patches is supplied according to the negative velocity feedback control strategy. Every actuator patch is equipped with a velocity sensor at its middle point to sense the transverse velocity ($\dot{w}^q$) at that point, and this velocity is feedback to the corresponding actuator patch in the form of a control voltage (V^q) with a control gain (k_d^q) as

$$V^q = -k_d^q \dot{w}^q. \tag{65}$$

The sensing-point velocity ($\dot{w}^q$) can also be expressed in terms of the global nodal velocity vector ($\dot{X}_p$) by introducing a transformation vector (N_T^q) as follows:

$$\dot{w}^q = N_T^q \dot{X}_p. \tag{66}$$

Using Eqs. (65)–(66), Eq. (64) can be expressed as

$$M\ddot{X}_p + (K_b + K_s)X_p = \left(-\sum_{q=1}^{4} C^q(\dot{w}^q) \right) \dot{X}_p + P_M(t),$$
$$C^q(\dot{w}^q) = \langle P_{Ec}^q(\dot{w}^q)k_d^q N_T^q \rangle. \tag{67}$$

In Eq. (67), $P_{Ec}^q(\dot{w}^q)$ can be obtained by introducing Eq. (1) in the expression of $P_E^q(V^q)$. Equation (67) can also be written in a simplified form as

$$M\ddot{X}_p + C_t \dot{X}_p + K_t X_p = P_M(t),$$
$$C_t = \sum_{q=1}^{4} C^q(\dot{w}^q), K_t = (K_b + K_s). \tag{68}$$

The damping matrix (C_t) in Eq. (68) signifies an electrically induced smart damping in the overall plate. For a linear relation between the electric field (E) and applied voltage (V) or for constant values of G_r, G_θ and G_z, the damping coefficient matrix (C_t) is independent of the sensing-point velocities ($\dot{w}^q$). Otherwise, it (C_t) would vary according to the velocities of the sensing points. In the present analysis, the control performance of presently designed smart actuator patches is assessed within a specified range of the driving frequency. Within that range of frequency, the simply supported ($v_o = 0$, $w_o = 0$, $\phi_\theta = 0$ at $r = r_i$, r_o) overall annular plate can vibrate in a shape of its first or second bending mode (Fig. 5). Since the actuator patches are attached to the top surface of the substrate plate, they act mainly against the mechanically induced radial stress (σ_r) on the same substrate surface for every mode of vibration. Now, for both modes (Fig. 5), the radial stress (σ_r) at the top substrate surface may not be distributed in uniform manner along the circumferential direction. So, for effective control of both the modes of vibration, the voltage to the actuator patches is to be supplied in
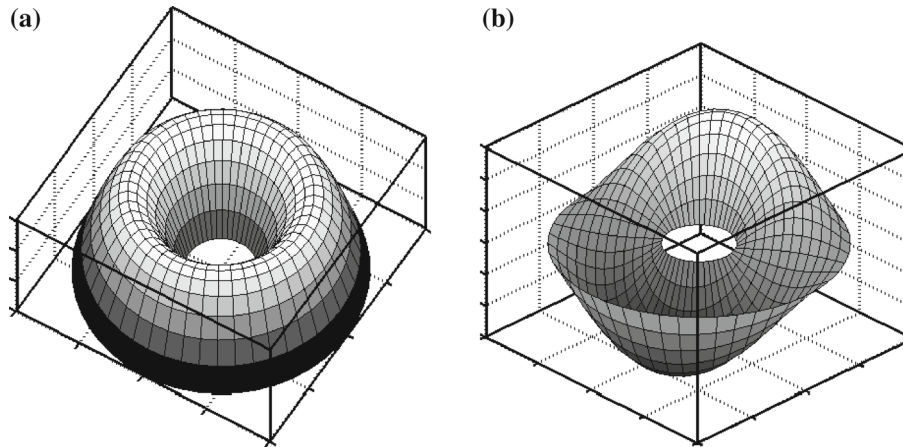
Fig. 5 a First and **b** second bending mode shapes of the simply supported overall annular plate

an adequate manner so that every actuator patch can act against the mechanically induced stress (σ_r) around its location. In order to conform this in the present use of velocity feedback control strategy, every actuator patch is equipped with a velocity sensor and activated according to the corresponding local velocity. As a consequence, one configuration (locations) of actuator patches may not be sufficient for effective control of all modes of vibration within a given range of driving frequency. But it (configuration) is to be utilized for the same purpose because of the physical infeasibility in shifting the patch configuration during operation of the overall plate within a range of the driving frequency. On this ground, the activation of actuator patches according to their local velocity facilitates to control several modes of vibration of the overall plate even though the patch configuration remains the same.

7 Results and discussion

In this section, first a numerical analysis of effective electro-elastic properties of present cylindrically orthotropic SPFRC is carried out for deciding the geometrical properties of a corresponding RVE with an objective of improved magnitude of the major effective piezoelectric coefficient (e_{11}). Next, the control performance of the SPFRC actuator is substantiated by the numerical evaluation of frequency responses of the simply supported annular substrate plate integrated with the same actuator patches. An associated issue of the change in control performance of such actuators (SPFRC) for using short piezoelectric fibers instead of continuous fibers (CPFRC) is also numerically evaluated.

7.1 Effective electro-elastic properties of SPFRC and CPFRC

Since the analysis of a similar cylindrically orthotropic SPFRC is not available in the literature, the present FE formulation in estimating the material constants is verified considering both the RVE and corresponding fiber in shape of a parallelepiped. If large values of inner and outer radii of present RVE (Fig. 1b) are considered along with a very small circumferential span, then the corresponding geometry of the RVE may be assumed as a parallelepiped. For a vertically poled continuous piezoelectric fiber within the RVE of such a geometrical shape, the effective electro-elastic coefficients are computed and compared with similar available results [22], which are estimated analytically for an RVE in shape of a perfect parallelepiped. This comparison is illustrated in Table 1. It may be observed from Table 1 that the present FE results are in good agreement with the earlier analytical results [22], thus verifying the present FE formulation for the evaluation of electro-elastic constants of piezoelectric composites.

The materials for fiber and matrix phases of the present cylindrically orthotropic SPFRC are considered as PZT5H and Epoxy, respectively. Table 2 presents the material properties of these constituent materials. For given constituent materials, the electro-elastic properties of SPFRC are mainly dependent on the area ratio (A_r) and length ratio (L_r) by the relation $v_f = (A_r \times L_r)$. Further, since the SPFRC acts as a material of distributed actuator by the application of an electric field along the poling direction of the fibers, the important

Table 1 Verification of the present FE formulation for an estimation of effective electro-elastic constants of piezoelectric composites ($*R_{31} = (e_{31})_{\text{composite}}/(e_{31})_{\text{piezoelectric fiber}}$)

v_f	Source	$*R_{31}$	C_{11} (GPa)	C_{12} (GPa)	C_{22} (GPa)
0.2	Present	0.6654	18.71	3.396	5.27
	Ray [22]	0.6859	17.93	3.191	4.794
0.4	Present	1.3334	34.55	4.752	6.62
	Ray [22]	1.3563	32.35	4.207	6.325
0.6	Present	1.9837	49.06	6.795	10.10
	Ray [22]	1.9902	47.63	6.177	9.293

Table 2 Material properties of constituent materials [22]

Fiber/matrix	C_{11} (GPa)	C_{12} (GPa)	C_{23} (GPa)	C_{22} (GPa)	C_{44} (GPa)
Epoxy	3.86	2.57	2.57	3.86	0.64
PZT-5H	124	96	98	151	26.5

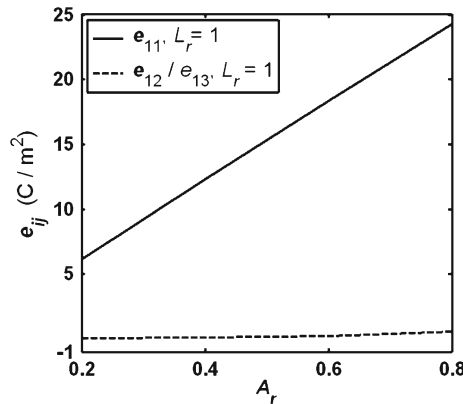| Fiber/matrix	e_{11} (C/m^2)	e_{12}/e_{13} (C/m^2)	e_{26}/e_{35} (C/m^2)	$\in_{11}$ (C/Vm $\times 10^{-09}$)	$\in_{22}$ / $\in_{33}$ (C/Vm $\times 10^{-09}$)
Epoxy	0	0	0	0.079	0.079
PZT-5H	27	-5.1	17	13.27	13.4

Fig. 6 Variations of effective piezoelectric coefficients (e_{11}, e_{12}, e_{13}) with the area ratio (A_r)

effective piezoelectric coefficients are e_{11}, e_{12} and e_{13}. So, the present analysis is carried out mainly for investigating the effects of these parameters (A_r, L_r) on the magnitudes of the effective coefficients e_{11}, e_{12} and e_{13}. Figure 6 represents the variations of the effective piezoelectric coefficients with the area ratio (A_r) for continuous piezoelectric fibers ($L_r = 1$). In order to achieve the variation of area ratio (A_r) for constant values of thickness (h_c) and circumferential span (θ_c) of the RVE, the fiber dimensions (h_f, θ_f) are varied following the relations $h_f = h_c\sqrt{A_r}$ and $\theta_f = \theta_c\sqrt{A_r}$. It may be observed from Fig. 6 that the magnitude of the effective coefficient (e_{11}) significantly increases with increasing area ratio. But the magnitude of the other coefficient (e_{12}/e_{13}) remains almost constant and it is also significantly lesser than the magnitude of e_{11}. This result signifies that the use of the smart composite as a material of distributed actuator would be based on the coefficient (e_{11}), and its magnitude can be increased by increasing the area ratio. However, for the use of short piezoelectric fibers ($L_r < 1$), the variations in the same coefficients (e_{11}, e_{12}, e_{13}) with the length ratio (L_r) are illustrated in Fig. 7 for different values of area ratio (A_r). In this computation, the fiber length is varied keeping the constant values of all other dimensions in such a manner that the central location of a short fiber within the RVE does not alter. For any value of area ratio (A_r), it may be observed form Fig. 7 that the magnitude of coefficient e_{11} significantly increases with the increasing length ratio (L_r) and reaches its (e_{11}) maximum value for $L_r = 1$ (continuous fiber). The other coefficient (e_{12}/e_{13}) also increases with increasing L_r. But, after a certain value of L_r, its (e_{12}/e_{13}) magnitude decreases to the minimum value for a continuous fiber ($L_r = 1$). Similar to the case of continuous fibers ($L_r = 1$, Fig. 6), the magnitude of e_{12}/e_{13} is much lesser than that of e_{11} (Fig. 7). Thus, for both the forms (short and continuous) of piezoelectric fibers within the present smart composite, the coefficient e_{11} would be chosen as the major piezoelectric coefficient in its (smart
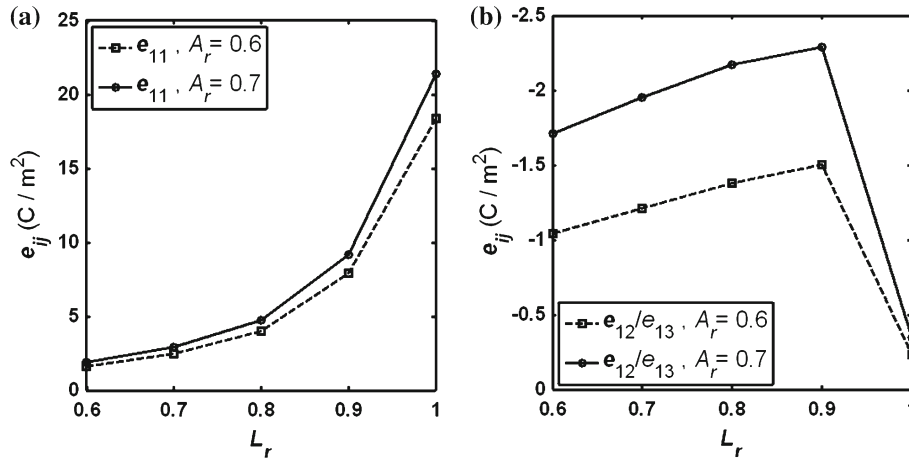
Fig. 7 Variations of the effective piezoelectric coefficients (e_{11}, e_{12}, e_{13}) with the length ratio (L_r) for different values of area ratio (A_r)

composite) use as a distributed actuator. In case of SPFRC, Fig. 7 indicates a higher value of L_r (close to 1) for improved magnitude of e_{11}. The same figure (Fig. 7) also indicates the significant effect of area ratio on the magnitude of e_{11} for a higher value of the length ratio. So, for SPFRC, higher values of both the area ratio and length ratio are to be considered for improved magnitude of e_{11}. However, based on the forgoing observations (Figs. 6, 7), a higher value of area ratio is chosen at present as 0.6 for both the SPFRC and CPFRC, while a higher value of length ratio for SPFRC is chosen as 0.95. Basically, the CPFRC is modified into a SPFRC by reducing the value of the length ratio from 1 to 0.95. This modification causes a little decrease in the magnitude of e_{11} (Fig. 7a) from its maximum possible magnitude (at $L_r = 1$). But an advantage of greater flexibility and conformability of the smart composite can be achieved which is useful in its structural applications.

Like area ratio and length ratio, the dimensions such as l_c, h_c and θ_c are also to be mentioned for complete geometrical properties of the present RVE. These dimensions (l_c, h_c, θ_c) of the RVE are directly related to the similar dimensions (l_f, h_f, θ_f) of the corresponding fiber by the relations $l_f = L_r l_c$, $h_f = h_c\sqrt{A_r}$ and $h_f = h_c\sqrt{A_r}$. So, the dimensions of the fiber could also be specified instead of those of the RVE. For the aforesaid selected values of area ratio and length ratio, the cross-sectional dimensions (h_f, θ_f) are considered to have small values as compared to the value of the longitudinal dimension (l_f). This consideration results in negligibly small effects of variations of these parameters (h_f, θ_f) on the magnitudes of the effective coefficients (e_{11}, e_{12}, e_{13}) when other geometrical parameters remain at their constant values. So, for simplicity, these dimensions (h_f, θ_f) could be represented by a single parameter, A_f ($A_f = h_f \theta_f$). Now, for specified values of A_r and L_r, the values of A_f and l_f may be assigned arbitrarily. But this arbitrary assignment may have an effect on the magnitudes of the effective coefficients (e_{11}, e_{12}, e_{13}) which implies a relation among these parameters (A_f, l_f) for improved magnitude of e_{11}. This relation is estimated at present by defining a parameter as fiber aspect ratio ($S_f = l_f/A_f$). In this computation, two values of A_r are considered by varying A_f with a constant value of A_c ($A_c = h_c\theta_c$, $A_r = A_f/A_c$). For every value of A_r or A_f, S_f is varied by the variation of l_f. It should be noted that the value of l_c would vary with l_f for constant value of L_r. Figure 8 illustrates the variations of the coefficients (e_{11}, e_{12}, e_{13}) with the fiber aspect ratio (S_f) for different values of the area ratio (A_r). It may be observed from Fig. 8 that there is a little variation of every coefficient ($e_{11}/e_{12}/e_{13}$) with the piezoelectric fiber aspect ratio (S_f) for any value of A_r/A_f. Also, the nature of variation of any of the coefficients (e_{11}, e_{12}, e_{13}) does not alter for different values of the area ratio. Thus, for specified values of area ratio and length ratio, the value of S_f can be chosen from this result (Fig. 8) and this is taken at present as 1.2×10^4 for an improved magnitude of e_{11}. However, according to the present geometrical properties (SPFRC, $L_r = 0.95$, $A_r = 0.6$, $S_f = 1.2 \times 10^4$) of the RVE, the effective electro-elastic properties are illustrated in Table 3. The same table also illustrates similar properties when the continuous piezoelectric fiber of an RVE is considered (CPFRC, $L_r = 1$, $A_r = 0.6$). It may be observed from Table 3 that the magnitude of the major effective piezoelectric coefficient (e_{11}) decreases for the use of short piezoelectric fibers ($L_r = 0.95$) instead of continuous fibers ($L_r = 1$). This decrease in the magnitude of e_{11} is an important issue when one intends to use an SPFRC actuator instead of a CPFRC actuator. However, the corresponding change in the control performance is studied in a latter section considering the aforesaid arrangement of surface electrodes.
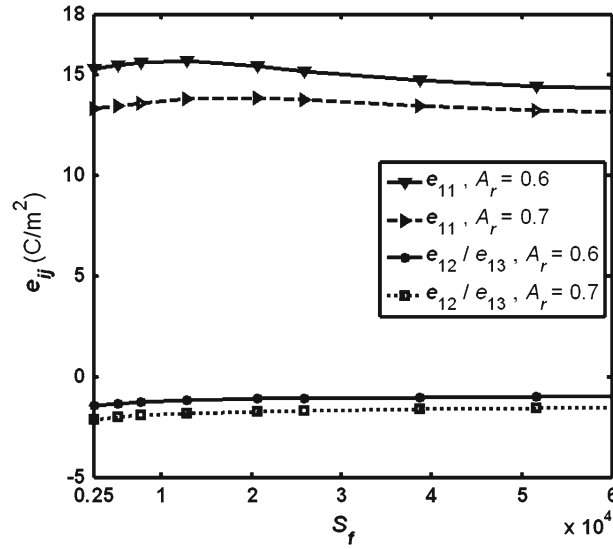
Fig. 8 Variations of effective piezoelectric coefficients (e_{11}, e_{12}, e_{13}) with the fiber aspect ratio (S_f) ($L_r = 0.95$)

Table 3 Effective electro-elastic properties of a cylindrically orthotropic PFRC with radially poled short/continuous piezoelectric fibers

Composite	e_{11} (C/m^2)	e_{12}/e_{13} (C/m^2)	e_{26}/e_{35} (C/m^2)	$\in_{11}$ (C/Vm)($\times 10^{-09}$)	$\in_{22}$ / $\in_{33}$ (C/Vm) ($\times 10^{-09}$)	
SPFRC	13.818	−1.158	1.220	0.95	0.302	
CPFRC	18.379	−0.231	1.429	8.75	0.28	

Composite	C_{11} (GPa)	C_{12} (GPa)	C_{23} (GPa)	C_{22} (GPa)	C_{44} (GPa)	C_{55} (GPa)
SPFRC	31.635	4.734	4.201	12.623	1.628	2.229
CPFRC	36.019	6.794	4.34	13.056	1.649	2.503

7.2 Electric field for the present arrangement of surface electrodes

The foregoing results show a significant magnitude of e_{11} for the present cylindrically orthotropic SPFRC/CPFRC. In order to utilize this piezoelectric coefficient in the use of the present SPFRC/CPFRC as a material of distributed actuator, an arrangement of surface electrodes is shown in Fig. 2. The corresponding volume-average electric field within the RVE is expressed as a function of applied voltage (V) according to Eq. (44). In this section, this functional relation is evaluated numerically. Figure 9 illustrates the variations of the radial component ($\overline{E}_r$) of volume-average electric field ($\overline{E}$) with the applied voltage (V) across the pairs of surface electrodes. As compared to the magnitude of $\overline{E}_r$, other components ($\overline{E}_\theta$, $\overline{E}_r$) have negligibly small magnitudes. So, these components ($\overline{E}_\theta$, $\overline{E}_z$) of the electric field ($\overline{E}$) are not furnished in the present results. However, it may be observed from Fig. 9 that the radial component of the electric field ($\overline{E}_r$) linearly varies with the applied voltage (V). Also, the magnitude of the slope ($\overline{E}_r$ vs. V) of this linear variation for SPFRC is more than that for CPFRC. According to this result (Fig. 9), the magnitudes of G_r for SPFRC and CPFRC are obtained as 540.65 m^{-1} and 369.55 m^{-1}, respectively. Since the other similar parameters (G_θ and G_z) have negligibly small magnitudes as compared to the magnitude of G_r, these parameters are considered to have null magnitudes ($G_\theta \approx 0$, $G_z \approx 0$).

7.3 Frequency responses of a smart annular plate

In this section, the control performance of a presently designed SPFRC actuator is assessed by analyzing the controlled frequency responses of a simply supported annular plate integrated with four identical actuator patches (Fig. 4). The controlled frequency responses of the overall smart annular plate are evaluated using its closed-loop FE model derived in Sect. 6. The geometrical properties of the overall annular plate are considered
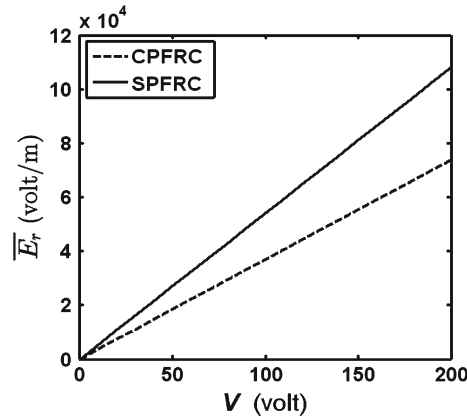
Fig. 9 Variations of the radial component ($\overline{E}_r$) of the volume-average electric field ($\overline{E}$) with the applied voltage (V) for SPFRC and CPFRC actuators

Table 4 Comparison of the first two dimensionless natural frequencies ($\Omega_0 = \omega_0 r_0 \sqrt{\rho h/D}$, $\Omega_1 = \omega_1 r_0 \sqrt{\rho h/D}$) of a simply supported annular plate ($h_p \approx 0$) with those given in [48] ($\nu = 1/$, $r_i/r_0 = 0.4$, $h/r_0 = 0.001$), $D = Eh^3/12(1 - \nu^2)$)

Source	Ω_0	Ω_1
Chakravarthy et al. [48]	28.08	30.09
Present	28.35	30.43

as $r_i = 0.25$ m, $r_o = 1$ m, $h = 4$ mm, $h_p = 250\,\mu$ m, $\beta = 60^{\rm o}$ and $\alpha = 30^{\rm o}$. The substrate annular plate is considered to be made of aluminum ($E = 70$ GPa, $\nu = 0.3$, $\rho = 2700$ kg/m^2), while the material properties of the smart actuator patches are tabulated in Table 3. The density of actuator patches is taken according to the rule of mixture ($\rho_{\rm c} = 3666$ kg/m^2). For linear relation between the electric field ($\boldsymbol{E}$) and the applied voltage (V) (Fig. 9), the damping coefficient matrix ($\boldsymbol{C}_t$) is independent of the sensing-point velocities ($\dot{w}^q$), and it yields linear governing equations of motion [Eq. (68)] of the overall smart annular plate. In order to excite the first two bending modes (Fig. 5) of the overall annular plate, the transversely distributed harmonic mechanical load is considered as

$$p(r, \theta, t) = p \langle 1 + \cos(\theta) \rangle e^{j\omega t}, \quad j = \sqrt{-1} \tag{69}$$

where p is the amplitude parameter of the distributed load and ω is the driving frequency. For the steady-state linear vibration of the overall plate under this mechanical excitation [Eq. (69)], the nodal displacement vector (X_p) can be written as [47]

$$X_p = \overline{X}e^{j\omega t}, \overline{X} = (X_R + jX_I) \tag{70}$$

where $\overline{X}$ is a complex nodal displacement vector and X_R/X_I is its real/imaginary counterpart. Substituting Eq. (70) in the linear form of the governing equations of motion [Eq. (68)], the following algebraic equations can be obtained:

$$\left(-\omega^2 \boldsymbol{M} + j\omega \boldsymbol{C}_t + \boldsymbol{K}_t\right) \overline{X} = \boldsymbol{P}_M^0. \tag{71}$$

The complex nodal displacement vector ($\overline{X}$) can be obtained by solving Eq. (71), and the absolute value of the same ($\overline{X}$) is the nodal amplitude vector for the linear steady-state vibration of the overall smart annular plate.

In order to verify the present FE model of a smart annular plate, the natural frequencies for the first two bending modes of vibration of the simply supported substrate annular plate ($h_p \approx 0$) are computed and compared with similar results available in the literature [48]. This comparison is illustrated in Table 4. Table 4 shows a good agreement of the present results with similar results reported in an earlier study [48]. This comparison verifies the accuracy of the present FE model for an annular plate. Next, the modeling of electro-elastic coupling is verified. Since a similar smart composite actuator is not available in the literature, this verification is carried out considering a substrate circular plate integrated with a vertically poled monolithic piezoelectric layer. A negligibly small thickness ($h \approx 0$) of the substrate plate is considered, and the transverse
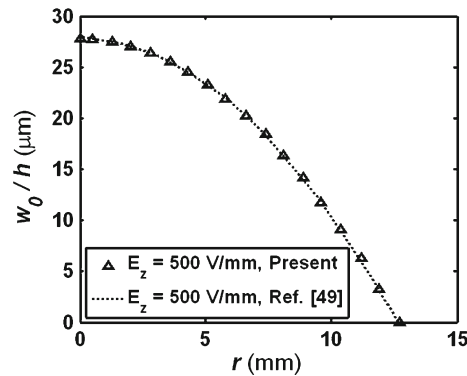
Fig. 10 Verification of the FE formulation for handling electro-elastic coupling in piezoelectric actuators

deflections at different radial locations of the simply supported overall smart circular plate are computed for an applied electric field across the top and bottom electrode surfaces of the piezoelectric layer. These results are then compared with those for a similar smart circular plate studied by Dong et al. [49]. Figure 10 illustrates this comparison, and it shows an excellent agreement of the present results with similar published results [49]. Thus, the present FE formulation is verified for handling the electro-elastic coupling in a piezoelectric actuator.

In order to present the frequency responses of the overall annular plate, the amplitude of flexural vibration (A_w) at a point $((r_o - r_i)/2, \pi/4, 0)$ on the plate is computed at every frequency and represented by $W = (A_w/h)$. The present smart composite actuators reduce the amplitude of vibration of the overall annular plate by inducing smart damping within the same (overall) plate. The maximum reduction in amplitude due to smart damping occurs at the resonant frequency for any mode of vibration. So, for every mode of vibration, the efficiency of actuators (SPFRC and CPFRC) in inducing smart damping within the overall plate is measured in terms of the change of peak amplitude (W_{peak}) at resonant frequency. All actuator patches are considered to be activated using a uniform value of control gain ($k_d^q = k_d$, q =1,2,3,4). But the velocity amplitudes corresponding to the locations of velocity sensors may be of different values. So, the control voltages for four actuator patches are computed separately at any frequency of vibration, and the maximum one (V^m) is taken at this frequency for presenting the numerical results.

Figure 11a demonstrates the frequency responses of the overall smart annular plate when the actuator patches are either made of SPFRC or made of CPFRC. The corresponding variations of control voltage (V^m) are also illustrated in Fig. 11b. It may be observed from Fig. 11 that the SPFRC/CPFRC induces significant damping in the overall annular plate in expense of reasonable control voltage. The smart damping in the overall plate can also be increased by increasing the value of control gain (k_d). But the corresponding required control voltage (V^m, Fig. 11b) remains almost the same mainly because of the constant value of the load parameter (p). For a particular value of control gain (k_d), Fig. 11 illustrates an important observation that the induced damping in the overall plate by CPFRC actuators is a little smaller than that by SPFRC actuators in expense of added control voltage (V^m). This may be due to the fact that the magnitude of the electric field induced in an SPFRC actuator due to an applied voltage is more than that in a CPFRC actuator (Fig. 9). The SPFRC actuator has lesser magnitude of major piezoelectric coefficient (e_{11}) as compared to that for a CPFRC actuator (Table 3). But the larger magnitude of induced electric field within it (SPFRC) as compared to that in a CPFRC actuator (Fig. 9) causes more damping within the overall plate in case of an SPFRC actuator. In order to exemplify this difference for every mode (first and second modes) of vibration, the variations of the peak amplitude (W_{peak}) either with the load parameter (p, constant value of k_d) or with the control gain (k_d, constant value of p) are presented in Figs. 12 and 13. Figure 12 illustrates the variations of the peak amplitude (W_{peak}) and corresponding control voltage (V_{peak}^m) with the load parameter (p) for a constant value of control gain ($k_d = 100$). Figure 13 demonstrates the variations of the same parameters (W_{peak}, V_{peak}^m) with the control gain (k_d) for a constant value of load parameter ($p = 0.3$ N/m^2). In comparison with the CPFRC actuator, it may be observed from Figs. 12 and 13 that the SPFRC actuator induces more damping in expense of lesser control voltage. This difference also increases as the value of W_{peak} increases either by increasing the value of the load parameter (p, constant value of k_d) or by reducing the value of control gain (k_d, constant value of p). However, from the foregoing observations (Figs. 11, 12, 13), it may be concluded that the control performance of the present cylindrically orthotropic smart composite actuator can be improved by the use of short piezoelectric fibers instead of similar fibers in continuous form. The use of short fibers
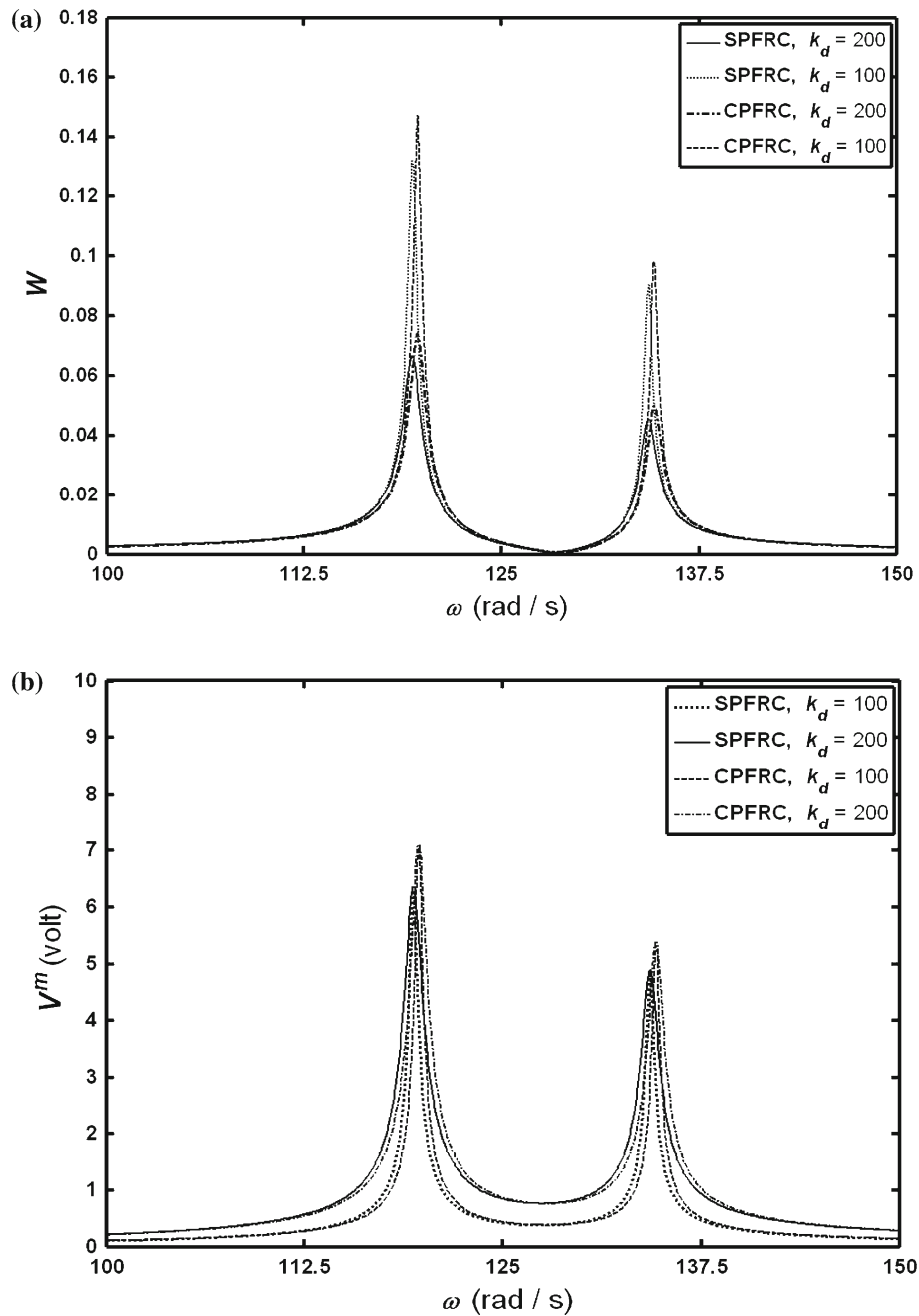
Fig. 11 a Controlled frequency responses of the annular plate integrated with the patches of an SPFRC/CPFRC actuator, **b** variations of corresponding control voltage ($p = 0.3\,\text{N/m}^2$, $k_d = 100, 200$)

instead of continuous fibers also facilitates to have a cylindrically orthotropic smart composite actuator with greater flexibility and conformability.

For constant values of load parameter (p) and control gain (k_d), Fig. 14 illustrates the variations of the peak amplitude (W_{peak}) and corresponding control voltage (V_{peak}^m) with the thickness (h_p) of the actuator patches for the first bending mode of vibration of the overall annular plate. For every value of h_p, W_{peak} is computed at the corresponding resonant frequency (for the first mode). It is known that a finite value of W_{peak} at a resonant frequency arises due to the existence of damping within the overall plate. So, the variations of W_{peak} in Fig. 14a represent the variation of damping within the overall annular plate with the increase in h_p. Figure 14a, b indicates that a significant damping within the overall annular plate in expense of a low value
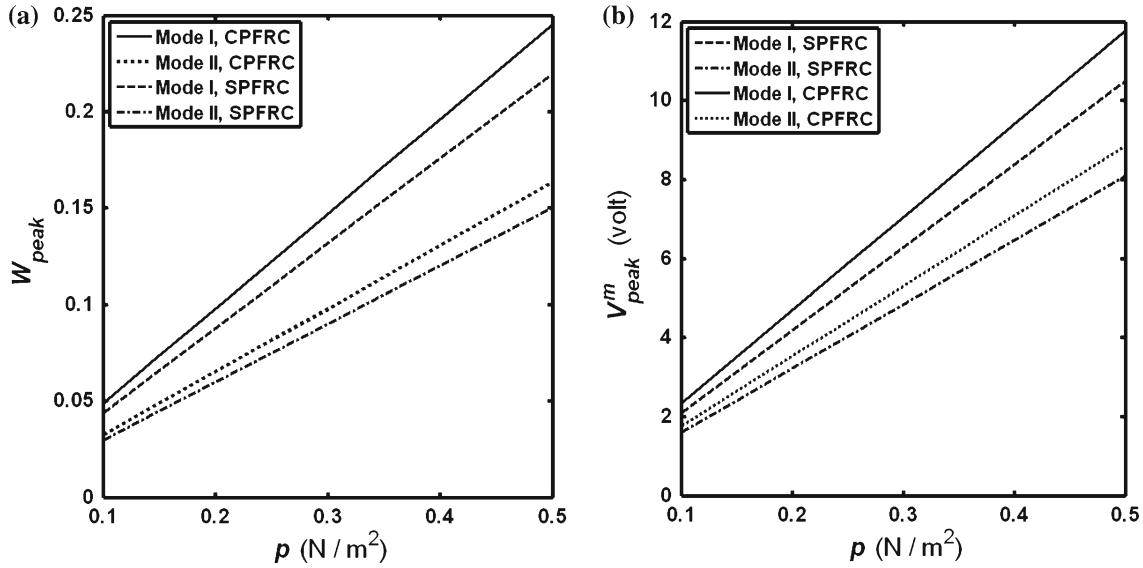
Fig. 12 Variations of **a** peak amplitude (W_{peak}) and **b** corresponding control voltage (V_{peak}^m) with the load parameter (p) for the first two bending modes of vibration of the overall annular plate ($k_d = 100$)
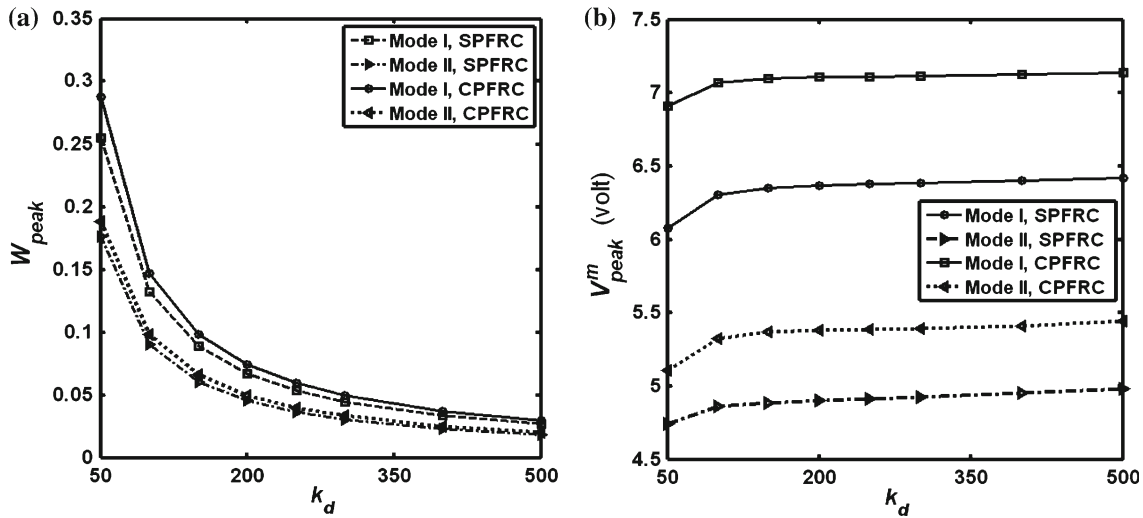

Fig. 13 Variations of **a** peak amplitude (W_{peak}) and **b** corresponding control voltage (V_{peak}^m) with control gain k_d for first two bending modes of vibration of the overall annular plate ($p = 0.3\,\text{N/m}^2$)

of control voltage could be achieved by increasing the thickness of the SPFRC/CPFRC actuator patches. But, for constant values of k_d and p, this increase in damping continues up to a certain value of increasing h_p. Beyond that value of h_p, the negligibly small rate of decrease in W_{peak} with increasing h_p (Fig. 14a) indicates an insignificant effect of h_p on the smart damping within the overall plate.

8 Conclusions

In the present work, a cylindrically orthotropic short piezoelectric fiber-reinforced composite (SPFRC) actuator is designed for active damping of the vibration of annular plates. The SPFRC is comprised of unidirectional short piezoelectric fibers embedded within the epoxy matrix. The unidirectional fibers are oriented in the radial direction within a reference cylindrical coordinate frame and poled in the same direction so as to achieve an improved magnitude of the effective piezoelectric coefficient (e_{11}, 1 for radial direction). For the use of this smart composite as a material of distributed actuator based on the effective coefficient (e_{11}), an arrangement of surface electrodes over the top and bottom surfaces of the smart composite layer is presented. Utilizing a
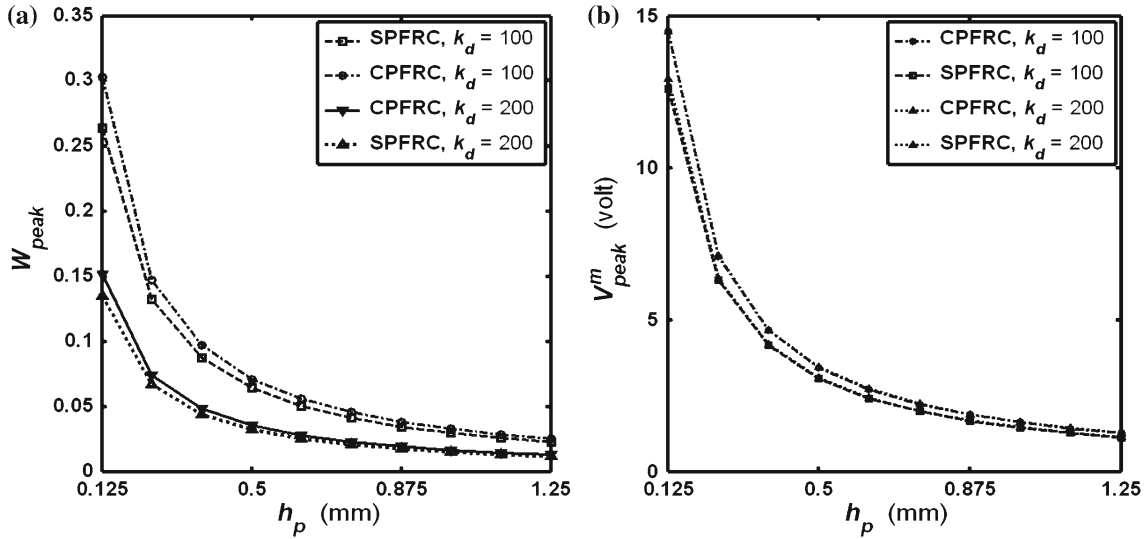
Fig. 14 Variations of **a** peak amplitude (W_{peak}) and **b** corresponding control voltage (V_{peak}^m) with actuator thickness (h_p) ($p = 0.3\,\text{N/m}^2$, $k_d = 100, 200$) for first bending mode of vibration of the overall annular plate

finite element procedure, the effective electro-elastic constants of the smart composite are evaluated for both the short (SPFRC) and continuous (CPFRC) forms of unidirectional piezoelectric fibers. In this evaluation of material constants, the geometrical properties of the corresponding RVE are also determined with an objective of improved magnitude of the effective coefficient (e_{11}). The numerical results reveal a significant magnitude of the effective coefficient (e_{11}) of the smart composite while other similar coefficients have negligibly small magnitudes. It is observed that the use of short fibers instead of continuous fibers causes a smaller magnitude of e_{11}.

The control performance of a presently designed cylindrically orthotropic SPFRC/CPFRC actuator is substantiated by the evaluation of frequency responses of an annular plate integrated with four identical patches of the same (SPFRC/CPFRC) actuators. The actuator patches are activated according to the negative velocity feedback control strategy so as to achieve smart damping in the overall annular plate. A closed-loop FE model of the overall smart annular plate is derived in order to evaluate its (overall plate) controlled frequency responses, which exhibit significant performance of both the actuators in inducing smart damping within the overall plate. It is observed that the special arrangement of surface electrodes causes a larger magnitude of volume-average electric field in an SPFRC actuator than that in a CPFRC actuator for an applied voltage. Because of this fact, the evaluated frequency responses of the smart annular plate show a little more control power of the SPFRC actuator than that of the CPFRC actuator although the magnitude of the concerned coefficient (e_{11}) for SPFRC is smaller than that for CPFRC. The overall study reveals significant control power of the present cylindrically orthotropic SPFRC/CPFRC actuator in control of the vibration of annular plates. Also, the use of short piezoelectric fibers instead of continuous piezoelectric fibers provides the advantages of greater control power, flexibility and conformability of the present smart actuator.

Appendix

$$
\boldsymbol{\epsilon}_f = \begin{bmatrix} \epsilon_{11}^f & 0 & 0 \\ 0 & \epsilon_{22}^f & 0 \\ 0 & 0 & \epsilon_{33}^f \end{bmatrix}, \quad \boldsymbol{\epsilon}_m = \begin{bmatrix} \epsilon_{11}^m & 0 & 0 \\ 0 & \epsilon_{22}^m & 0 \\ 0 & 0 & \epsilon_{33}^m \end{bmatrix}, \quad \boldsymbol{e}_f = \begin{bmatrix} e_{11} & e_{12} & e_{13} & 0 & 0 & 0 \\ 0 & 0 & 0 & 0 & 0 & e_{26} \\ 0 & 0 & 0 & 0 & e_{35} & 0 \end{bmatrix},
$$

$$
\boldsymbol{C}_f = \begin{bmatrix} C_{11}^f & C_{12}^f & C_{13}^f & 0 & 0 & 0 \\ C_{21}^f & C_{22}^f & C_{23}^f & 0 & 0 & 0 \\ C_{31}^f & C_{32}^f & C_{33}^f & 0 & 0 & 0 \\ 0 & 0 & 0 & C_{44}^f & 0 & 0 \\ 0 & 0 & 0 & 0 & C_{55}^f & 0 \\ 0 & 0 & 0 & 0 & 0 & C_{66}^f \end{bmatrix}, \quad \boldsymbol{C}_m = \begin{bmatrix} C_{11}^m & C_{12}^m & C_{13}^m & 0 & 0 & 0 \\ C_{21}^m & C_{22}^m & C_{23}^m & 0 & 0 & 0 \\ C_{31}^m & C_{32}^m & C_{33}^m & 0 & 0 & 0 \\ 0 & 0 & 0 & C_{44}^m & 0 & 0 \\ 0 & 0 & 0 & 0 & C_{55}^m & 0 \\ 0 & 0 & 0 & 0 & 0 & C_{66}^m \end{bmatrix}, \quad \text{(A.1)}
$$

$$
L = \begin{bmatrix}
\frac{\partial}{\partial r} & \frac{1}{r} & 0 & 0 & \frac{\partial}{\partial z} & \frac{1}{r}\frac{\partial}{\partial \theta} & 0 & 0 & 0 \\
0 & \frac{1}{r}\frac{\partial}{\partial \theta} & 0 & \frac{\partial}{\partial z} & 0 & \frac{\partial}{\partial r} - \frac{1}{r} & 0 & 0 & 0 \\
0 & 0 & \frac{\partial}{\partial z} & \frac{1}{r}\frac{\partial}{\partial \theta} & \frac{\partial}{\partial r} & 0 & 0 & 0 & 0 \\
0 & 0 & 0 & 0 & 0 & 0 & \frac{\partial}{\partial r} & \frac{1}{r}\frac{\partial}{\partial \theta} & \frac{\partial}{\partial z}
\end{bmatrix}^{\mathrm{T}},
\tag{A.2}
$$

$$
L_{bt} = \begin{bmatrix}
\partial/\partial r & 0 & 0 & 0 & 0 \\
1/r & (1/r)(\partial/\partial \theta) & 0 & 0 & 0 \\
(1/r)(\partial/\partial \theta) & (\partial/\partial r) - (1/r) & 0 & 0 & 0
\end{bmatrix},
\tag{A.3}
$$

$$
L_{br} = \begin{bmatrix}
0 & 0 & 0 & \partial/\partial r & 0 \\
0 & 0 & 0 & 1/r & (1/r)(\partial/\partial \theta) \\
0 & 0 & 0 & (1/r)(\partial/\partial \theta) & (\partial/\partial r) - (1/r)
\end{bmatrix},
\tag{A.4}
$$

$$
L_s = \begin{bmatrix}
0 & 0 & \partial/\partial r & 1 & 0 \\
0 & 0 & (1/r)(\partial/\partial \theta) & 0 & 1
\end{bmatrix},
\tag{A.5}
$$

$$
C_b^k = \frac{E}{1 - \nu^2}\begin{bmatrix}
1 & \nu & 0 \\
\nu & 1 & 0 \\
0 & 0 & \frac{1-\nu}{2}
\end{bmatrix}, \quad
C_s^k = \frac{E}{1 + \nu}\begin{bmatrix}
1/2 & 0 \\
0 & 1/2
\end{bmatrix}, \; k = 1,
\tag{A.6}
$$

$$
C_b^k = \begin{bmatrix}
C_{11}^k & C_{12}^k & 0 \\
C_{12}^k & C_{22}^k & 0 \\
0 & 0 & C_{66}^k
\end{bmatrix}, \quad
C_s^k = \begin{bmatrix}
C_{55}^k & 0 \\
0 & C_{44}^k
\end{bmatrix}, \; k = 2,
\tag{A.7}
$$

$$
e_b^{\mathrm{T}} = \begin{bmatrix}
e_{11} & 0 & 0 \\
e_{12} & 0 & 0 \\
0 & e_{26} & 0
\end{bmatrix}, \quad
e_s^{\mathrm{T}} = \begin{bmatrix}
0 & 0 & e_{35} \\
0 & 0 & 0
\end{bmatrix},
\tag{A.8}
$$

$$
\epsilon = \begin{bmatrix}
\epsilon_{11} & 0 & 0 \\
0 & \epsilon_{22} & 0 \\
0 & 0 & \epsilon_{33}
\end{bmatrix},
\tag{A.9}
$$

$$
Z_t = \begin{bmatrix}
1 & 0 & 0 & 0 & 0 \\
0 & 1 & 0 & 0 & 0 \\
0 & 0 & 1 & 0 & 0
\end{bmatrix}, \quad
Z_r = \begin{bmatrix}
0 & 0 & 0 & z & 0 \\
0 & 0 & 0 & 0 & z \\
0 & 0 & 0 & 0 & 0
\end{bmatrix}.
\tag{A.10}
$$

References

1. Bailey, T., Hubbard, J.E., James, E.: Distributed piezoelectric polymer active vibration control of a cantilever beam. J. Guid. Control Dyn. **8**, 605–611 (1985)
2. Miller, S.E., Hubbard, J.E.: Observability of a Bernoulli–Euler beam using PVF2 as a distributed sensor. In: MIT Draper Laboratory Report (July 1987)
3. Crawley, E.F., Luis, J.D.: Use of piezoelectric actuators as elements of intelligent structures. AIAA J. **25**, 1373–1385 (1987)
4. Baz, A., Poh, S.: Performance of an active control system with piezoelectric actuators. J. Sound Vib. **126**, 327–343 (1988)
5. Hui, L.H.: Axisymmetric response of circular plates with piezoelectric layers: exact solutions. Int. J. Mech. Sci. **40**, 1265–1289 (1998)
6. Lee, C.Y., Huang, R., Li, X., Shih, W.H.: Vibrations and static responses of asymmetric bimorph disks of piezoelectric ceramics. IEEE Trans. Ultrason. Ferroelectr. Freq. Control **47**, 706–715 (2000)
7. Dong, S., Tong, L.: Vibration control of plates using discretely distributed piezoelectric quasi-modal actuators/sensors. AIAA J. **39**, 1766–1772 (2001)
8. Liu, X., Wang, Q., Quek, S.T.: Analytical solution for free vibration of piezoelectric coupled moderately thick circular plates. Int. J. Solids Struct. **39**, 2129–2151 (2001)
9. Ray, M.C.: Optimal control of laminated shells with piezoelectric sensor and actuator layers. AIAA J. **41**, 1151–1157 (2003)
10. Sekouri, E.M., Yan-Ru, H., Ngo, A.D.: Modeling of a circular plate with piezoelectric actuators. Mechatronics **14**, 1007–1020 (2004)
11. Peng, F., Ng, A., Hu, Y.R.: Actuator placement optimization and adaptive vibration control of plate smart structures. J. Intell. Mater. Syst. Struct. **16**, 263–271 (2005)
12. Fox, C.H.J., Chen, X., McWilliam, S.: Analysis of the deflection of a circular plate with an annular piezoelectric actuator. Sens. Actuators **133**, 180–194 (2007)
13. Ashida, F., Sakata, S., Matsumoto, K.: Structure design of a piezoelectric composite disk for control of thermal stress. ASME J. Appl. Mech. **75**, 610091–0610098 (2008)
14. Cook, A.C., Vel, S.S.: Multiscale analysis of laminated plates with integrated piezoelectric fiber composite actuators. Compos. Struct. **94**, 322–336 (2012)
15. Prasanth, S.S., Arockiarajan, A.: Effective electromechanical response of macro-fiber composite (MFC): analytical and numerical models. Int. J. Mech. Sci. **77**, 98–106 (2013)
16. Wilkie, W.K., Inman, D.J., Lloyd, J.M., High, J.W.: Anisotropic laminar piezocomposite actuator incorporating machined PMN–PT single-crystal fibers. J. Intell. Mater. Syst. Struct. **17**, 15–28 (2006)
17. Smith, W.A., Auld, B.A.: Modeling of 1-3 composite piezoelectrics: thickness mode oscillations. IEEE Trans. Ultrason. Ferroelectr. Freq. Control **38**, 40–47 (1991)
18. Huang, J.H., Kuo, W.-S.: Micromechanics determination of the effective properties of piezoelectric composites containing spatially oriented short fibers. Acta Mater. **44**, 4889–4898 (1996)

19. Bent, A.A., Hagood, N.W.: Piezoelectric fiber composites with interdigitated electrodes. J. Intell. Mater. Syst. Struct. **8**, 903–919 (1997)
20. High, J.W., Wilkie, W.K.: Method of fabricating NASA-standard macro-fiber composite piezoelectric actuators. In: National Aeronautics and Space Administration, Langley Research Center (2003)
21. Mallik, N., Ray, M.C.: Effective coefficients of piezoelectric fiber reinforced composites. AIAA J. **41**, 704–710 (2003)
22. Ray, M.C.: Micromechanics of piezoelectric composites with improved effective piezoelectric constant. Int. J. Mech. Mater. Des. **3**, 361–371 (2006)
23. Shu, D., Della, C.N.: The performance of 1–3 piezoelectric composites with a porous non-piezoelectric matrix. Acta Mater. **56**, 754–761 (2008)
24. Chakaraborty, D., Kumar, A.: Effective properties of thermo-electro-mechanically coupled piezoelectric fiber reinforced composites. Mater. Des. **30**, 1216–1222 (2009)
25. Arockiarajan, A., Sakthivel, M.: Thermo-electro-mechanical response of 1–3–2 piezoelectric composites: effect of fiber orientations. Acta Mech. **223**, 1353–1369 (2012)
26. Kalamkarov, A.L., Savi, M.A.: Micromechanical modeling and effective properties of the smart grid reinforced composites. J. Braz. Soc. Mech. Sci. Eng. **XXXIV**, 343–351 (2012)
27. William, K.W., Robert, G.B., James, W.H., Robert, L.F., Richard, F.H., Anthony, J. Jr., Bruce, D.L., Paul, H.M.: Low-cost piezocomposite actuator for structural control applications. In: Proceedings of SPIE 3991, Smart Structures and Materials 2000: Industrial and Commercial Applications of Smart Structures Technologies **323** (2000)
28. Park, S., Inman, D.J., Yun, C.B.: An outliner analysis of MFC-based impedance sensing data for wireless structural health monitoring of railroad tracks. Eng. Struct. **30**, 2792–2799 (2008)
29. Choi, S.C., Park, J.S., Kim, J.H.: Active damping of rotating composite thin-walled beams using MFC actuators and PVDF sensors. Compos. Struct. **76**, 362–374 (2006)
30. Kovalovs, A., Barkanov, E., Gluhihs, S.: Active control of structures using macro-fiber composite (MFC). J. Phys. Conf. Ser. **93**, 012034 (2007)
31. Bilgen, O., Kochersberger, K.B., Inman, D.J., Ohanian, O.J.: Macro-fiber composite actuated simply supported thin airfoils. Smart Mater. Struct. **19**, 055010 (2010)
32. Bent, A.A.: Active fiber composite material systems for structural control applications. In: Proceedings of SPIE 3674, Smart Structures and Materials 1999: Industrial and Commercial Applications of Smart Structures Technologies **166**, (1999)
33. Sodano, H.A., Park, G., Inman, D.J.: An investigation into the performance of macro-fiber composites for sensing and structural vibration applications. Mech. Syst. Signal Process. **18**, 683–697 (2004)
34. Sohn, J.W., Kim, H.S., Choi, S.B., Kim, K.S.: Experimental investigation of smart hull structures based on macro fiber composite actuators. Key Eng. Mater. **326**, 1419–1422 (2006)
35. Azzouz, M.S., Bevan, J.S., Ro, J.-J., Mei, C.: Finite element modeling of MFC/AFC actuators. In: Proceedings of SPIE 326: Smart Structures and Materials 2001: Modeling, Signal Processing, and Control in Smart Structures (2001)
36. Ray, M.C., Reddy, J.N.: Performance of piezoelectric fiber-reinforced composites for active structural acoustic control of laminated composite plates. IEEE Trans. Ultrason. Ferroelectr. Freq. Control **51**, 1477–1490 (2004)
37. Ikeda, T.: Fundamentals of Piezoelectricity. Oxford University Press, Oxford (1990)
38. Dunn, M.L., Taya, M.: Micromechanics predictions of the effective electroelastic moduli of piezoelectric composites. Int. J. Solids Struct. **30**, 161–175 (1993)
39. Furukawa, T.: Piezoelectricity and pyroelectricity in polymers. IEEE Trans. Electr. Insul. **24**, 375–395 (1989)
40. Cady, W.G.: Piezolectricity. McGraw-Hill, New York (1946)
41. Hasin, Z.: Viscoelastic behavior of heterogeneous media. J. Appl. Mech. **32**, 630 (1965)
42. Hasin, Z.: Complex moduli of viscoelastic composites-I, general theory and application to particulate composites. Int. J. Solids Struct. **6**, 539–552 (1970)
43. Aboudi, J., Arnold, S.M., Bednarcyk, B.A.: Micromechanics of Composite Materials. Academic Press, New York (2013)
44. Odegard, G.M.: Constitutive modeling of piezoelectric polymer pomposities. Acta Mater. **52**, 5315–5330 (2004)
45. Tiersten, H.F.: Linear Piezoelectric Plate Vibrations. Plenum, New York (1969)
46. Cook, R.D., Malkus, D.S., Plesha, M.E., Witt, R.J.: Concepts and Applications of Finite Element Analysis. Wiley, New York (2001)
47. Meirovitch, L.: Elements of Vibration Analysis. McGraw-Hill, New York (2007)
48. Chakraverty, S., Bhat, R.B., Stiharu, I.: Free vibration of annular elliptic plates using boundary characteristic orthogonal polynomials as shape functions in the Rayleigh–Ritz method. J. Sound. Vib. **241**, 524–539 (2001)
49. Dong, S., Uchino, K., Li, L., Viehland, D.: Analytical solutions for the transverse deflection of a piezoelectric circular axisymmetric unimorph actuator. IEEE Trans. Ultrason. Ferroelectr. Freq. Control **54**, 1240–1248 (2007)